CHALMERS
UNIVERSITY OF TECHNOLOGY

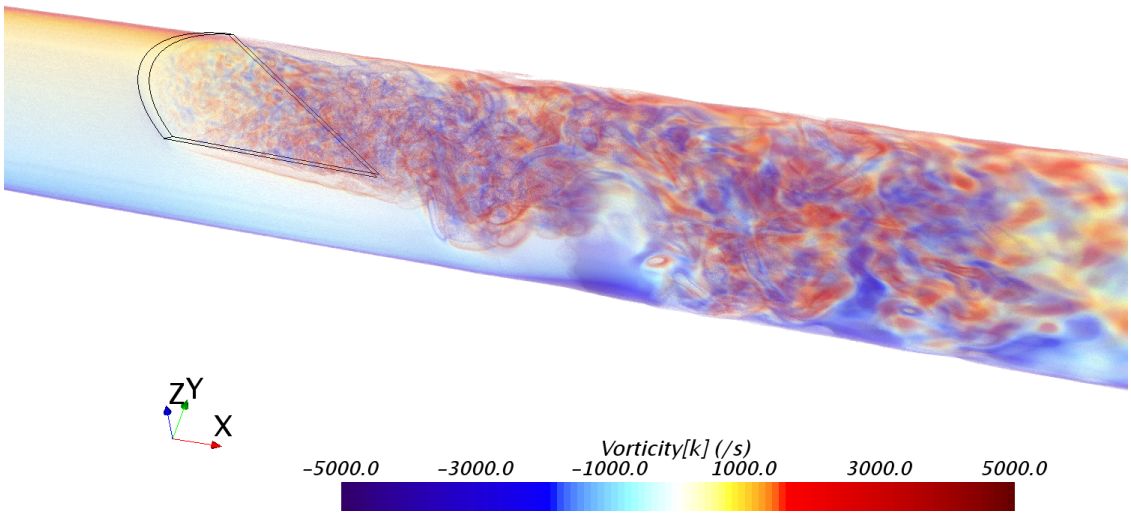

On the Effect of Flexibility for In-Duct Plates with Focus on Aeroacoustics

An Incompressible Computational Fluid Dynamics Study Using Fluid-Structure Interaction and Applying a Dipole Approximation of Curle's Acoustic Analogy

Master's thesis in Applied Mechanics

MAGDALENA JANSSON
MÄRTA ÅBLAD

Department of Applied Mechanics
CHALMERS UNIVERSITY OF TECHNOLOGY
Gothenburg, Sweden 2016

Master's thesis 2016:14

On the Effect of Flexibility for In-Duct Plates with Focus on Aeroacoustics

An Incompressible Computational Fluid Dynamics Study Using Fluid-Structure Interaction and Applying a Dipole Approximation of Curle's Acoustic Analogy

MAGDALENA JANSSON
MÄRTA ÅBLAD

CHALMERS
UNIVERSITY OF TECHNOLOGY

Department of Applied Mechanics
Division of Fluid Dynamics
Chalmers University of Technology
Gothenburg, Sweden 2016

On the Effect of Flexibility for In-Duct Plates with Focus on Aeroacoustics
An Incompressible Computational Fluid Dynamics Study Using Fluid-Structure Interaction and Applying a Dipole Approximation of Curle's Acoustic Analogy
MAGDALENA JANSSON, MÄRTA ÅBLAD

Supervisor: Dr. Mikael Karlsson, Escenda Engineering AB
Examiner: Prof. Lars Davidson, Applied Mechanics

Master's Thesis 2016:14
ISSN 1652-8557
Department of Applied Mechanics
Division of Fluid Dynamics
Chalmers University of Technology
SE-412 96 Gothenburg
Telephone +46 31 772 1000

Cover: Transparent isosurfaces of the z-component of vorticity around the stiff plate in a part of the computational domain

Typeset in LaTeX
Gothenburg, Sweden 2016

On the Effect of Flexibility for In-Duct Plates with Focus on Aeroacoustics
An Incompressible Computational Fluid Dynamics Study Using Fluid-Structure Interaction and Applying a Dipole Approximation of Curle's Acoustic Analogy
MAGDALENA JANSSON
MÄRTA ÅBLAD
Department of Applied Mechanics
Chalmers University of Technology

Abstract

The flow of air around an angled steel plate in a duct generates noise. Previous experimental studies show that the noise is reduced if the plate is allowed to be flexible, however the underlying mechanisms are not fully understood. Therefore it is desirable to find an accurate and affordable numerical solution to the problem. In this thesis, the stiff and the flexible plate are simulated using the commercial CFD software Star CCM+. Sound generation is then estimated by applying a dipole approximation of Curle's acoustic analogy. The results show that the velocity field and sound generation can be accurately predicted for the stiff plate and that the Star CCM+ FSI solver accurately predicts the plate motion. However, the sound reduction for the flexible plate is not captured. The reason for the discrepancies between simulation and experiments in terms of sound generation are unclear, however the motion of the plate is believed to make the dipole sound approximation an unsuitable approach.

Keywords: CFD, FSI, aeroacoustics, Curle's acoustic analogy, vortex mixer plate, noise reduction.

Acknowledgements

This master's thesis was carried out during the spring term of 2016, and represents the final step towards the Master of Science in Engineering (civilingenjör) degree for both authors. The period has been one of hard work, confusion, insight and excellent team work. However, our closely knit working duo also owes its gratitude to a number of other persons.

A warm thank you to our supervisor Mikael Karlsson and to our colleague Haukur Hafsteinsson at Escenda, and to Axel Kierkegaard at CD-adapco for sharing knowledge and experience, and for showing enthusiasm for our work.

The simulation work could not have been carried out without the generous provision of licenses from CD-adapco, or without the unselfish loan of computational resources from Volvo Car Corporation where Johan Brunberg with ample patience kept our simulations running, informing us whenever problems occured.

Thank you also to Escenda for fruit and friendliness, to the Fluid Division at Chalmers for the past two years of helping hands, and to our friends and families for being the best.

Magdalena Jansson and Märta Åblad, Gothenburg, June 2016

Contents

Nomenclature

Latin

a	Speed of sound
A	Area
b_i	Body load
C_D	Drag coefficient
C_{ijkl}	Stiffness tensor
f_i	External force
f_{V_i}	External volume forces
$\hat{f}$	Fourier transform
F	Force
F_D	Drag force
$\hat{G}_{xx}$	Autospectral density function
$\hat{G}_{xy}$	Cross-spectral density function
He	Helmholtz number
i	Imaginary unit
k	Wave number
ℓ	Characteristic length
L_p	Sound pressure level
M	Mach number
n_d	Number of time sequences
p	Pressure
p_0	Reference pressure
r	Radial distance
Re	Reynolds number
St	Strouhal number
t	Time
T_{ij}	Lighthill tensor
u	Velocity in x-direction
u^+	Non-dimensional velocity
x	Spatial coordinate
$\mathbf{x}$	Position vector in space
$\mathbf{x}_s$	Source position vector
X	Displacement of solid element

y	Spatial coordinate
y^+	Non-dimensional wall distance
z	Spatial coordinate

Greek

γ_{xy}	Coherence
ε_{ij}	Strain tensor
μ	Dynamic viscosity
ν	Kinematic viscisity
ξ	Fourier transform variable
ρ	Density
σ	Standard deviation
σ_{ij}	Cauchy stress tensor
τ_{ij}	Viscous stress tensor
τ_w	Wall shear stress
ω	Angular frequency

Acronyms

CAD	-	Computer-Aided Design
CFD	-	Computational Fluid Dynamics
CPU	-	Central Processing Unit
DES	-	Detached Eddy Simulation
DFT	-	Discrete Fourier Transform
DNS	-	Direct Numerical Simulation
FEM	-	Finite Element Method
FFT	-	Fast Fourier Transform
FSI	-	Fluid-Structure Interaction
LES	-	Large Eddy Simulation
PSD	-	Power Spectral Density
RANS	-	Reynolds-Averaged Navier-Stokes
SPL	-	Sound Pressure Level
URANS	-	Unsteady Reynolds-Averaged Navier-Stokes

List of Figures

List of Tables

1
Introduction

In this thesis, sound induced by a triangular plate in a duct is simulated. The plate is treated as both stiff and flexible, where the latter case requires the use of Fluid-Structure Interaction (FSI). For both simulation results, a dipole approximation of an acoustic analogy is used to estimate the generated sound. The results are validated using available experimental data.

1.1 Background

It is commonly known that unsteady flow can create noise; this is the idea behind musical instruments such as flutes, as well as the main reason why it is difficult to construct a silent air conditioning fan. In many applications the noise is undesired, which has made aeroacoustics an increasingly important research topic.

A specific area where noise control is of large interest is within the automotive industry. An overall reduction of sound includes controlling noise generated by external flow (i.e. the flow of air around the vehicle) as well as the noise from internal sources such as pipes within the engine.

In 2008, experiments of sound generation were performed for a triangular plate in a circular duct, a geometry which can be interpreted as a mixer plate in the exhaust system of a vehicle. From the experiments it was concluded that the use of a flexible plate significantly reduced the generated noise at the dominating frequencies, compared to the use of a stiff plate [1]. Supplementary measurements are performed presently; some were presented in [2], and others are yet to be published [3]. The experimental results have also been used for validation of non-commercial codes [4, 5].

1.2 Aim

The aim of the present work is to numerically investigate the same in-duct plate case that has previously been investigated experimentally, using the commercial Computational Fluid Dynamics (CFD) software Star CCM+. First, a simulation is performed where the plate is treated as stiff. The sound is estimated by an acoustic analogy, more specifically a 1D dipole approximation of Curle's equation, applied to a duct. This is the same approach to sound estimation that has been employed in previous simulation studies. Secondly, a case which is identical to the first, with the single exception of the plate being thinner and treated as flexible, is investigated. For this simulation, FSI has to be included. The case also provides a

good opportunity to validate the FSI solver of Star CCM+. Sound is estimated in the same way as in the stiff plate case, and the results are compared to each other and to experimental data. The two previous cases are performed for the same velocity. The stiff plate is also simulated for a higher velocity to investigate how the sound scales with velocity.

Finally, the physical factors behind the sound generation for this case remain somewhat undetermined. An increased understanding of the mechanisms present could be helpful in a future attempts to reduce noise. Therefore some different attempts at understanding the flow features related to sound generation are included in the present work.

1.3 Scope

All of the flow fields used to estimate sound generation are obtained through CFD simulations in the commercial software Star CCM+ version 11.02.009. There are two plate thicknesses, and hence two different sets of plate properties: a 3 mm plate which is considered stiff and a 0.5 mm plate which is considered flexible. Three different simulations are performed: for the stiff plate two velocities are simulated and for the flexible plate the lower of those velocities is simulated. Incompressible flow is assumed for all simulations, gravity is neglected and an acoustic analogy is used to estimate sound from the numerical solutions.

2

Theory

In this chapter, theory relevant for understanding of the thesis is presented. The main focus is aeroacoustics, but the chapter also treats fluid and solid mechanics, computational fluid dynamics, fluid-structure interaction and signal processing.

2.1 Fluid Dynamics

The study of moving fluids is known as fluid dynamics. The governing equations in fluid dynamics in their present form were developed by Navier and Stokes in the late 19^{th} century [6]. For the case of incompressible flow the Navier-Stokes equations in Cartesian tensor notation read

$$\begin{cases} \dfrac{\partial u_i}{\partial x_i} = 0 \\ \dfrac{\partial u_i}{\partial t} + u_j \dfrac{\partial u_i}{\partial x_j} = -\dfrac{1}{\rho}\dfrac{\partial p}{\partial x_i} + \nu \dfrac{\partial^2 u_i}{\partial x_j \partial x_j} + f_i \end{cases} \tag{2.1}$$

where u denotes fluid velocity, p pressure, t time, x spatial coordinate, ρ density, ν kinematic viscosity and f external forces such as gravity.

Depending on the flow characteristics, different simplifications can come into question. In the above formulation, the assumption of incompressible flow has already been made. It is thus considered valid as long as the velocity normalized by the speed of sound, also known as the Mach number[(1)], is below the limit of 0.3 [6]. Further simplifications can be made depending on the nature of the flow. A mean of assistance in predicting and understanding the flow is to consider different dimensionless numbers.

The most important such number is the Reynolds number[(2)], which is the ratio between the inertial and the viscous forces in the flow. For low Re, a flow can be considered to be laminar. For laminar flow and simple geometries, Equations 2.1 can be solved analytically. However, what can be seen as a low Re differs between applications; most flows in both nature and industrial applications are high Re turbulent flows.

[(1)] Mach number $M = \dfrac{u}{a}$, where a is speed of sound.

[(2)] Reynolds number $Re = \dfrac{\rho u \ell}{\mu}$, where μ is the dynamic viscosity of the fluid and ℓ is some characteristic length scale of the flow domain.

2.1.1 Turbulence

The complex nature of turbulence is evident from the fact that although it is present in the lion's share of flows, there is no formal definition of it. The following characteristics are often used to describe turbulence:

- **Irregular:** the flow is unsteady and partly random, making it difficult to predict.
- **Diffusive:** the turbulent fluctuations make all quantities involved spread faster than in laminar flows.
- **Wide range of scales:** the variation of both length and time scales of turbulent structures is considerable.
- **Three dimensional:** turbulent structures and fluctuations are always three dimensional by nature.

Here, the term fluctuation refers to the deviation from the mean value [7]. Another word frequently used when discussing turbulence is eddy, designating a turbulent feature which has a length scale and a time scale.

2.1.2 Computational Fluid Dynamics

Since analytical solutions to Equations 2.1 are seldom available, either experimental or numerical approaches are usually needed to achieve the relevant flow physics. Both approaches have their advantages, but with recent technological advances the use of numerical techniques, known as Computational Fluid Dynamics (CFD), has increased substantially. Commercial CFD solvers are often based on finite volume techniques, where the domain is split into smaller control volumes and the discretized Navier-Stokes equations solved for each one of them [8].

To fully resolve turbulent flow, the cell size has to be of the same order of magnitude as the smallest turbulent length scales, and the time step has to be as small as the smallest time scale. This type of simulation is known as Direct Numerical Simulation (DNS) and, although yielding quite accurate results, requires so much computational power and time that it is not used in industrial applications today. Instead, different turbulence models are used to model all or a portion of the scales. The choice of model depends on flow type, geometry, computational resources and desired outcome [7].

2.1.2.1 Reynolds-Averaged Navier-Stokes

Different types of averaging are frequently used to simplify Equations 2.1. The loss of information entailed is less of a problem in applications where the mean properties are of most interest, which is often the case in industry. The Reynolds-Averaged Navier-Stokes equations (RANS) are based on a time average of Equations 2.1; the velocity and the pressure are decomposed into a mean and a fluctuating part which are inserted into the equations before averaging. A new term, known as the Reynolds stress tensor, appears, adding six new unknowns to the equations which thereby become unclosed. A number of models such as the $k-\varepsilon$ and the $k-\omega$ models have been developed to close the problem. As mentioned above, turbulence is always

unsteady and thus the Reynolds stress tensor can be seen as a representation of the interaction between the mean flow and turbulence [7, 9].

For flows where the temporal variation is important, RANS appears to be too coarse a method. However, if the averaging of the Navier-Stokes equation is performed using an ensemble average instead of a time average, the Unsteady Reynolds-Averaged Navier-Stokes (URANS) equations are obtained. Although these equations include an unsteady momentum equation term, they still do not resolve turbulence but rely on models to account for its influence [9, 10].

2.1.2.2 Large Eddy Simulation

Another possibility of simplifying the Navier-Stokes equations is by using a method based on a spatial average. This method is known as Large Eddy Simulation (LES). Here, it is assumed that a separation of scales can be made: all eddies larger than some threshold length are resolved, while the influence of smaller structures is modelled using a so called subgrid scale model. Again, the spatial averaging or filtering will result in an unclosed term, the subgrid stress tensor, representing the mentioned subgrid scale turbulence influence. As in the RANS case, the problem is closed by modelling this term [7].

2.1.2.3 Detached Eddy Simulation

When the accuracy of URANS is not enough to capture relevant flow features, but the computational resources are insufficient for LES, a hybrid method can be used. Detached Eddy Simulation (DES) combines URANS close to walls with LES further away from walls, whereby only the eddies detached from boundary layers are resolved. The reason for using URANS close to solid walls is that the complexity of the flow in the boundary layer, where gradients are high and viscous effects important, lead to excessive grid requirements in this region [7].

2.1.2.4 Wall Treatment

To further alleviate the requirements on the mesh size in boundary layers, wall functions are often used. These are based on the assumption of a fully developed turbulent velocity profile (i.e. a profile that does not change with the streamwise direction) close to the wall. The boundary layer can then be divided into three different regions, using the dimensionless wall distance[3] y^+. The innermost region is known as the viscous sublayer. In this region, which extends to $y^+ \approx 5$, the velocity corresponds linearly to the distance from the wall. From $y^+ \approx 30$, and above, the velocity profile is approximately a logarithmic function of the wall distance. As a result, this range is known as the log law region. Between the two, i.e. from $y^+ \approx 5$ to $y^+ \approx 30$, neither approximation holds. This region is called the buffer layer, and smoothly connects the two other regions. An illustration of the normalized velocity[4] u^+ as a function of the dimensionless wall distance y^+ is given in Figure 2.1 [6, 9].

[3] Dimensionless wall distance $y^+ = \frac{y\sqrt{\tau_w/\rho}}{\nu}$, where τ_w is the wall shear stress

[4] Dimensionless velocity $u^+ = \frac{u}{\sqrt{\tau_w/\rho}}$, where τ_w is the wall shear stress

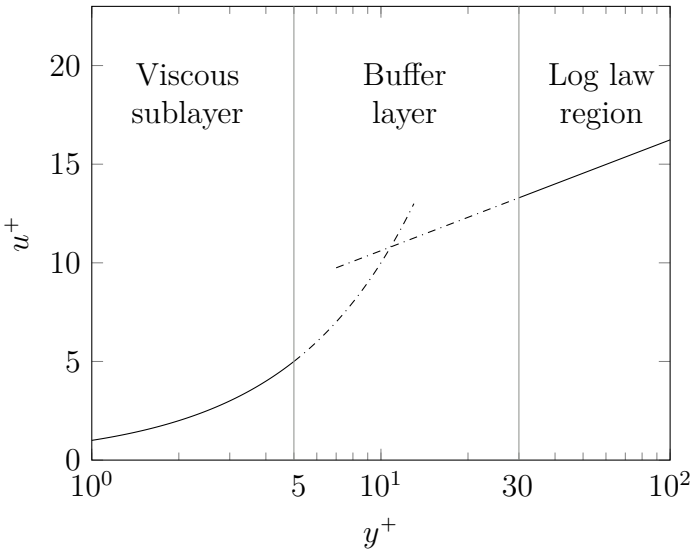

Figure 2.1: The three theoretical regions of a fully developed turbulent boundary layer. Note that the x-axis has a logarithmic scale. Details on the linear and logarithmic laws can be found in [6].

The type of wall function used depends on in which of the regions the node closest to the wall is placed. Typically, either a low y^+ treatment ($y^+ < 5$)[5] or a high y^+ treatment ($y^+ \gtrsim 30$) is applied. Combinations where the mesh size determines what model to use are also possible [9, 11].

2.1.3 Drag Coefficient

A fluid moving around a body gives rise to forces and moments. The force component parallel to the free stream direction is commonly defined as the drag force. This force causes a flow loss present in all flows, irrespective of body shape and flow properties. The omnipresence of the drag force has lead to the definition of a dimensionless number, the drag coefficient, to quantify it for different objects. The drag coefficient is generally defined as

$$C_D = \frac{F_D}{\frac{1}{2}\rho u^2 A} \tag{2.2}$$

where F_D is the drag force, ρ is the fluid density and A is an area suitable for the problem at hand [6]. Equation 2.2 can be applied to an in-duct object as

$$C_D = \frac{\Delta p A_{\text{duct}}}{\frac{1}{2}\rho u^2 A_{\text{proj}}} \tag{2.3}$$

where Δp is the difference in pressure upstream and downstream of the object, when effects of other influences on the pressure have been removed, A_{duct} is the area of the duct and A_{proj} is the area of the object projected in the flow direction [2].

[5] In Star CCM+, $y^+ \lesssim 1$

2.2 Solid Mechanics

Solid material is, naturally, ruled by other governing equations. Here, only the equations that belong to the subcategory of *linear elastic isotropic* material will be treated. The assumption of elastic material, valid only for small deformations, means that the body will return to its original configuration when all loads are removed. Linearity implies that there is a linear relation between the stress and the strain of the material, making Hooke's law a valid constitutive relation. Finally, the term isotropic means that the material properties are the same in all directions [12]. Under these assumptions, the governing equations for solid displacement, known as the equilibrium equation, read

$$\rho\frac{\partial^2 X_i}{\partial t^2} - \frac{\partial \sigma_{ji}}{\partial x_j} - b_i = 0 \tag{2.4}$$

where X denotes displacement of a solid element (hence $\frac{\partial^2 X_i}{\partial t^2}$ is acceleration) and b any body load per unit volume [11, 13]. It should be noted that the Cauchy stress tensor σ_{ij} is dependent on X; first of all Hookes law gives that

$$\sigma_{ij} = C_{ijkl}\varepsilon_{kl} \tag{2.5}$$

where C_{ijkl} is a forth order stiffness tensor. Since linearity is assumed, the components of the stiffness tensor do not depend on the state of the material [13]. Then the linear strain tensor reads

$$\varepsilon_{ij} = \frac{1}{2}\left(\frac{\partial X_i}{\partial x_j} + \frac{\partial X_j}{\partial x_i}\right), \tag{2.6}$$

and gives a measure of how much the body has deformed [12]. Thus Equation 2.4 is more complicated than it might appear at first glance.

2.2.1 Finite Element Method

For most industrial applications, the equilibrium equation with boundary conditions is too demanding to be solved analytically. Instead, Equation 2.4 can be multiplied by a test function that fulfils certain criteria. It is then integrated over the solid domain. The new version of the problem is known as the weak formulation, and it can be shown that it is equivalent to the original formulation. Now, approximating the (continuous) solid displacement by a (discrete) weighted sum of basis functions, and choosing said basis functions one at a time as the test function, the so called Finite Element formulation is obtained.

This approximate version of the original problem can be solved numerically in an efficient way. The accuracy of the solution depends on the quality of the mesh but also on the order of the test functions. For further details, see any textbook on the Finite Element Method (FEM), such as [14].

2.2.2 Modal Analysis

Determining the characteristics of the dynamics of a solid structure in terms of its *modal data* can provide useful insight into its behaviour. Finding this data, which consists of the natural frequencies, the damping factors and the mode shapes of a structure, is the purpose of a modal analysis. This topic has become increasingly important in engineering contexts during the past 20 years, and one application is to verify that a mathematical model, such as a finite element model, corresponds to the structure which it attempts to represent [15].

2.3 Fluid-Structure Interaction

In problems where a significant dependence between fluid and structural mechanics exist, the Fluid-Structure Interaction (FSI) must be considered. On the interface between media, fluid pressure can lead to deformations of a structure and in return a displacement of a solid will affect the motion of a fluid. An FSI analysis can be one-way or two-way coupled. In one-way coupled problems, only the effect of one medium on the other is considered. This is usually a good approximation in systems where no large deformations occur, or where a solid structure moves without deforming. In two-way coupling, each medium's effect on the other is of importance [11].

Two-way coupled FSI solvers are divided into loosely coupled and strongly coupled algorithms. In loosely coupled problems solutions can be found sequentially: for each time step the fluid governing equations, the solid governing equations and the mesh movement are solved, in that order. In strongly coupled problems, on the other hand, the three equations are solved simultaneously, making it fully-coupled. The latter is more robust, but also requires more computational resources [11, 16].

2.4 Aeroacoustics

Sound can be induced by fluids moving over bodies. This is studied in aeroacoustics, which is a field that combines fluid dynamics and acoustics.

2.4.1 Acoustics

Sound is essentially weak pressure waves, governed by the homogeneous three dimensional wave equation

$$\frac{\partial^2 p}{\partial x_i^2} = \frac{1}{a^2}\frac{\partial^2 p}{\partial t^2} \tag{2.7}$$

where a is the speed of sound. Additional source terms can be introduced in Equation 2.7, making it inhomogeneous.

The strength of sound is usually expressed in dB, into which the varying pressure is converted by calculating the Sound Pressure Level (SPL)

$$L_P = 20 \log_{10}\left(\frac{\tilde{p}}{p_0}\right) \tag{2.8}$$

where $\tilde{p}$ is the root mean square-value of the pressure fluctuations and $p_0 = 2{\cdot}10^{-5}$ Pa is a reference pressure that roughly corresponds to the threshold of human hearing [17].

2.4.2 Lighthill's Acoustic Analogy

In numerics, fluctuating pressure can be transformed into sound using either a direct approach or an acoustic analogy. The direct approach is straight forward but computationally demanding: it requires solving the compressible Navier-Stokes equations, using a grid resolution fine enough to capture the acoustic pressure waves and a domain large enough to avoid boundary effects. The acoustic analogy, on the other hand, indirectly estimates sound from flow simulations to a far-field observer.

The first acoustic analogy was proposed by Lighthill in 1952. He rewrote the compressible Navier-Stokes equations in a form which can be interpreted as the inhomogeneous wave equation with sources.

The compressible version of Equations 2.1 reads

$$\begin{cases} \dfrac{\partial \rho}{\partial t} + \dfrac{\partial (\rho u_i)}{\partial x_i} = m \\ \dfrac{\partial (\rho u_i)}{\partial t} + \dfrac{\partial (\rho u_i u_j)}{\partial x_j} = -\dfrac{\partial p}{\partial x_i} + \dfrac{\partial \tau_{ij}}{\partial x_j} + f_{V_i} \end{cases} \tag{2.9}$$

where τ_{ij} is the viscous stress tensor and f_V denotes external volume forces. The first equation governs conservation of mass and the second conservation of momentum. Differentiating the conservation of mass with respect to time and the conservation of momentum with respect to space, and then taking the difference between the two gives

$$\frac{\partial^2 \rho}{\partial t^2} - \frac{\partial^2 p}{\partial x_i \partial x_i} = \frac{\partial m}{\partial t} - \frac{\partial f_{V_i}}{\partial x_i} + \frac{\partial^2}{\partial x_i \partial x_j}(\rho u_i u_j - \tau_{ij}). \tag{2.10}$$

Then, the decomposition $p = p_0 + p'$ and $\rho = \rho_0 + \rho'$ is introduced[6]. Adding $\dfrac{1}{a^2}\dfrac{\partial^2 p'}{\partial t^2}$ to both sides of Equation 2.10, and rearranging some terms, a form of the wave equation is obtained:

$$\frac{1}{a^2}\frac{\partial^2 p'}{\partial t^2} - \frac{\partial^2 p'}{\partial x_i \partial x_i} = \frac{\partial}{\partial t}\left(m + \frac{1}{a^2}\frac{\partial}{\partial t}(p' - a^2\rho')\right) - \frac{\partial f_{V_i}}{\partial x_i} + \frac{\partial^2}{\partial x_i \partial x_j}(\rho u_i u_j - \tau_{ij}). \tag{2.11}$$

This is the acoustic analogy: the left hand side represents the wave equation, and the right hand side represents monopole, dipole and quadrupole source terms respectively. Solving Equation 2.11 gives the fluctuating pressure based on the governing equations of fluid dynamics. The sound waves themselves have not been resolved, but rather the sources which give rise to the sound. It should be noted that the sound's effect on the flow is neglected.

Equation 2.11 can be simplified further. First of all, the term $(p' - a^2\rho')$, which corresponds to deviance from adiabatic changes of state, can be neglected if no heat release is present in the flow. The monopole term then only consists of change in

[6] Subscript 0 denotes the reference value and superscript $'$ denotes a fluctuation

mass flow, which can be neglected if there is no mass flow injection. The dipole term includes the spacial derivative of the volume force, which is zero when there are no volume forces present. Given these assumptions, only the quadrupole source term is left. Solving Equation 2.11 with respect to pressure gives

$$p'(x,t) = \iiint_V \frac{\partial^2}{\partial x_i \partial x_j} \left(\frac{T_{ij}(\mathbf{x}_s, t - r/a)}{4\pi r} \right) dV_{x_s} \tag{2.12}$$

where $T_{ij} = \rho u_i u_j - \tau_{ij}$ is known as the Lighthill tensor, r is radial distance and $\mathbf{x}_s$ denotes source position vector. The viscous stress τ_{ij} has negligible importance for sound production, and can also be neglected. The simplified expression of the Lighthill acoustic analogy becomes[7] [18]

$$p'(x,t) = \iiint_V \frac{\partial^2}{\partial x_i \partial x_j} \left(\frac{\rho u_i u_j}{4\pi r} \right) dV_{x_s}. \tag{2.13}$$

2.4.3 Curle's Equation

To include the effect of stationary solid bodies, an extension of Lighthill's analogy known as Curle's equation can be derived. Equation 2.13 can be rewritten using the Kirchhoff-Helmholtz equation, the free field Green's function and the equation of motion. A detailed description of the procedure can be found in e.g. [18]. The resulting equation reads

$$\begin{aligned} p'(\mathbf{x},t) = &\iiint_V \frac{\partial^2}{\partial x_i \partial x_j} \left[\frac{\rho u_i u_j}{4\pi r} \right]_{t_e} dV_{x_s} \\ &- \oiint_S \frac{\partial}{\partial x_i} \left[\frac{p n_i + \rho u_i u_j n_j}{4\pi r} \right]_{t_e} dS_{x_s} + \oiint_S \frac{\partial}{\partial t} \left[\frac{\rho u_i n_i}{4\pi r} \right]_{t_e} dS_{x_s} \end{aligned} \tag{2.14}$$

where $\mathbf{x}$ is the position vector and $t_e = t - \frac{r}{a}$ is emission time, i.e. the time required for a signal to travel from the source to the observer. Via these mathematical manipulations the quadrupole source term of Equation 2.13 has been rewritten into three different sources. The last integral is a monopole source connected to vibrationally induced volume flow, which in many cases can be neglected. Also assuming that the body is acoustically compact[8] Curle's equation simplifies to

$$p'(\mathbf{x},t) = \iiint_V \frac{\partial^2}{\partial x_i \partial x_j} \left[\frac{\rho u_i u_j}{4\pi r} \right]_{t_e} dV_{x_s} - \frac{\partial}{\partial x_i} \left(\frac{F_i(t - x/a)}{4\pi x} \right) \tag{2.15}$$

where $F_i(t) = \oiint_S p(\mathbf{x}_s, t) n_i dS_{x_s}$ is the fluctuating force that the body excerts on the fluid.

[7] u_i and u_j are still functions of the source coordinate $\mathbf{x}_s$ and the time $t - r/a$, however to increase readability of the equations this is no longer explicitly stated

[8] I.e. small compared to the wavelength of the generated sound

It can be shown that, for small Mach number, the dipole source will be the dominating term and hence Curle's equation is reduced to

$$p'(\mathbf{x},t) = -\frac{\partial}{\partial x_i}\left(\frac{F_i(t-x/a)}{4\pi x}\right). \tag{2.16}$$

In addition the assumption of small Mach numbers implies that the flow can be considered incompressible [18].

2.4.4 The Dipole Sound Approximation

Equation 2.16 states that generated sound can be approximated from the instantaneous pressure loss and that the dipole is the dominating source term. The expression can be further simplified by approximating the dipole source as a 1D dipole in the plane wave range. The sound field generated in a semi-infinite duct can then be expressed as

$$\tilde{p}_{\pm}(x) = \pm\frac{\tilde{F}e^{-ik_{\pm}x}}{2A_{\text{duct}}(1\pm M)} \tag{2.17}$$

where $\tilde{F}$ is the time varying dipole force and the $+$ and $-$ subscripts denote upstream and downstream propagation directions respectively. As the wave propagation speed is infinite for incompressible flow[(9)], Equation 2.17 simplifies to

$$\Delta\tilde{p} = \tilde{p}_{+} - \tilde{p}_{-} = \frac{\tilde{F}}{A_{\text{duct}}} \tag{2.18}$$

which is the dipole sound approximation. Solving the flow numerically, the force per area, $\frac{\tilde{F}}{A_{\text{duct}}}$, is by definition equal to the time varying pressure difference over the body. This pressure loss, averaged over the cross section area, can therefore be interpreted as the acoustic pressure [4].

2.4.5 Comparability to Experiments

When sound generation is investigated experimentally, the active part of the acoustics, which represents sound generated by the flow, can be measured upstream and downstream of the sound source. The sound is then expressed in terms of the autospectra, see Section 2.5.2, of the generated noise upstream (G^s_{11}) and downstream (G^s_{22}) [1, 2]. Estimating sound from an incompressible flow simulation, however, the sound can not be divided into an upstream and a downstream propagating wave. Consequently, if the dipole sound approximation is used to estimate sound, it can not be compared to the upstream or downstream experimental sound. However since Equation 2.18 gives a measure of the total sound generated, it can be argued that it corresponds to the sum of the sound measured in the experiments ($G^s_{11} + G^s_{22}$).

2.5 Signal Processing

A signal, here meaning a time dependent data series, can be analyzed using a number of different mathematical and statistical tools. Some of these are described below.

[(9)] Implying that $M = 0$ and $k = 0$

2.5.1 Fourier Transform

In Fourier analysis, the basic assumption is that any signal can be written as a sum of sinusoidal functions with different frequencies and amplitudes. This implies that it is possible to transform the signal from the time domain to the frequency domain, a procedure known as Fourier transform. The continuous Fourier transform is defined as

$$\hat{f}(\xi) = \int_{-\infty}^{\infty} f(x) e^{-i\xi x} dx. \tag{2.19}$$

where $f(x)$ is the time dependent signal. The Discrete Fourier Transform (DFT) is the equivalent of the Fourier transform, but for discrete valued signals such as the pressure fluctuation or spatial displacement of a point. The DFT of a data series $\{a_n\}_{n=0}^{N}$ with length N is defined as

$$\hat{a}_m = \sum_{n=0}^{N-1} e^{-2\pi i m n/N} a_n. \tag{2.20}$$

The DFT can be computed more efficiently. The most common algorithm for this is the Fast Fourier Transform (FFT), which has become widely used for numerical Fourier analysis [19].

Normally, the Fourier transform is computed assuming an infinitely long signal, which is never available for a numerical data series. When computing the DFT, it is thus assumed that the signal available will repeat itself. This means that the signal start and the signal end need to match to avoid undesired noise in the frequency domain. To enforce a match, a smoothing can be applied. The type of smoothing is categorized in terms of different windowing techniques, where no smoothing corresponds to a rectangular window. A commonly used window is the Hanning window, based on a multiplication of the signal by a cosine function [20].

2.5.2 Power Spectral Density

The autospectral density function, also known as the autospectral density or the Power Spectral Density (PSD), is defined as the Fourier transform of the auto-correlation function and provides similar information[(10)]. The autospectral density function can be estimated according to

$$\hat{G}_{xx}(f) = \frac{2}{n_d T} \sum_{k=1}^{n_d} |\hat{f}_k(f, T)|^2 \tag{2.21}$$

where $\hat{f}_k(f, T)$ is a Fourier transform evaluated in the limited range of $(0, T)$ instead of $(-\infty, \infty)$ as in Equation 2.19. This corresponds to averaging the square of the DFT over a number n_d of time sequences of length T, requiring a total signal length of $n_d T$ [20]. The sequence length T affects the frequencies resolvable, where large T increases the resolution. A larger number of sequences n_d reduces numerical noise and gives a clearer view of dominating trends.

[(10)] Such as if the compontents of a signal repeat themselves, and if so, with what time lags

To increase the efficiency and reduce the impact of the partitioning of the interval, the Welch method can be used to compute an estimate of the PSD. The method uses Equation 2.21 but also applies windowing, and overlapping of subintervals reducing the possible information loss caused by this [21].

2.5.3 Cross-spectral Density Function

In the same way as the autospectral density function can be used to study how a signal correlates with itself, the cross-spectral density function or cross power spectral density, defined as

$$\hat{G}_{xy}(f) = \frac{2}{n_d T} \sum_{k=1}^{n_d} \hat{f}_k^*(f,T)\hat{g}_k(f,T) \tag{2.22}$$

where * denotes complex conjugate, can be used to estimate the correlation between two different signals with finite Fourier transforms $\hat{f}_k$ and $\hat{g}_k$ [20]. Unlike the power spectral density, which is always real, $\hat{G}_{xy}$ can also contain an imaginary part. This means that the argument of $\hat{G}_{xy}(f)$, which corresponds to the phase shift of the frequency component f between the two signals, can be non-zero [22].

2.5.4 Coherence Function

To normalize the measure of similarity of two signals, the ordinary coherence function $\hat{\gamma}_{xy}^2(f)$ can be used. The coherence relates the autospectral density to the cross spectral density via

$$\hat{\gamma}_{xy}^2(f) = \frac{|\hat{G}_{xy}(f)|}{\hat{G}_{xx}(f)\hat{G}_{yy}(f)}. \tag{2.23}$$

Trivially, $0 \leqslant \hat{\gamma}_{xy}^2 \leqslant 1$ [20].

3
Methods

This chapter is centered around the simulations. First the set-up of the fluid and solid simulations are presented in separate sections, and then the combined problem is treated. In the end of the chapter, the practical aspects of the post-processing are explained.

3.1 Geometry

The computational domain consists of a circular duct, in which a triangular plate is inserted with a certain angle. The measurement specifications used to construct the domain were found in [2], where the diameter of the pipe $D = 90$ mm and the plate is mounted with an angle of 32°. The length of the duct was defined in terms of pipe diameters and set to -3.5D upstream and 20D downstream of the plate respectively, see Figure 3.1. At this length it was assumed that the boundaries would have negligible effect on the flow in important regions. The dimensions of the triangular plate, also from [2], are visualized in Figure 3.2. Simulations were carried out for two different geometries, identical except for the plate thickness: a 3 mm plate, which was considered stiff, and a 0.5 mm plate, which was modelled as flexible. The thicknesses were chosen in order to make the cases as comparable as possible to the experiments.

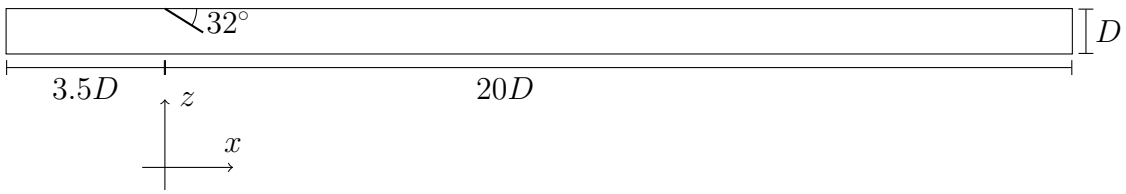

Figure 3.1: Two dimensional overview of the computational domain. The pipe diameter $D = 90$ mm. The line with the angle specification represents the plate. The flow is in the positive x direction, and the coordinate system is defined such that the point $x = 0$ is located at the most upstream contact between the plate and the duct wall, while $y = 0$ and $z = 0$ are positioned at the centerline of the duct.

The geometry for the fluid computational domain was created using the CAD software Catia v5. It was then exported in the form of a step file which was imported into Star CCM+ as a surface mesh. The built in feature *Surface Repair* was then used to define important surfaces and, in the flexible plate case, create

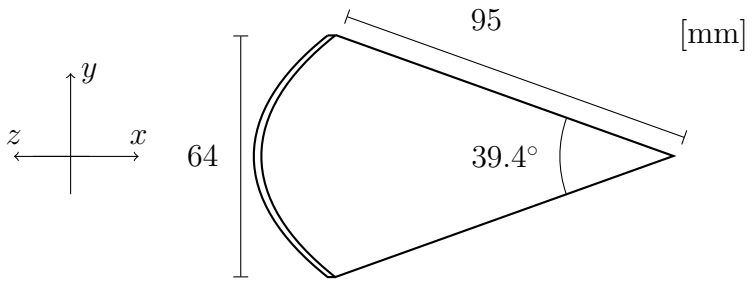

Figure 3.2: The plate, with the back (as defined in Figure 3.3) facing upwards. The rounded edge is connected to the upper duct wall. The plate thickness is 3 mm or 0.5 mm, depending on the case. Note that $y = 0$ at the symmetry plane of the plate.

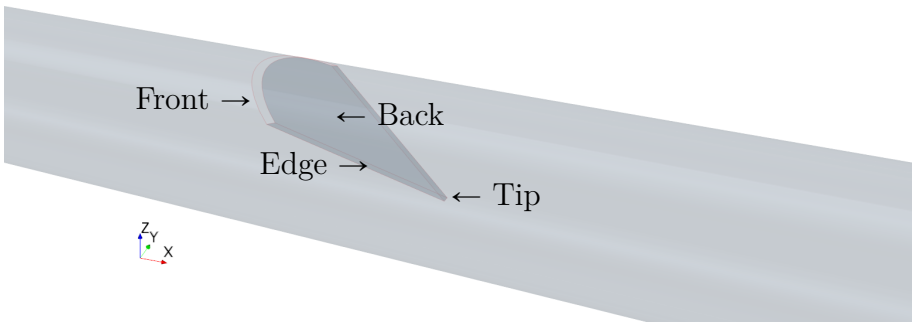

Figure 3.3: A 3D view of a part of the computational domain, including the names of important geometrical features.

a geometric part for the plate. The resulting computational domain is shown in Figure 3.3.

3.2 Modelling of Fluid Domain

Air at ambient conditions was chosen as the working fluid in the duct, and the STAR CCM+ predefined properties ($\rho = 1.18415\text{kg/m}^3$, $\mu = 1.85508 \cdot 10^{-5}$ Pa/s) were used. The flow was assumed to be incompressible and gravity was neglected. Two different velocities, $M = 0.125$ and $M = 0.188$, were simulated.

3.2.1 Computational Mesh

The mesh was created using the Polyhedral Mesher together with the Advancing Layer Mesher and the Surface Remesher. In the greater part of the domain the Base size[(1)] of the polyhedrons was set to 0.002 m. To improve the accuracy, a volumetric refinement with a Base size of 0.001 m was introduced around and downstream of the plate. The refinement was confined to a cylinder ranging from $x = -0.25D$ to

[(1)]The Base size is a characteristic length of the problem, and is not directly correlated to the size of cells

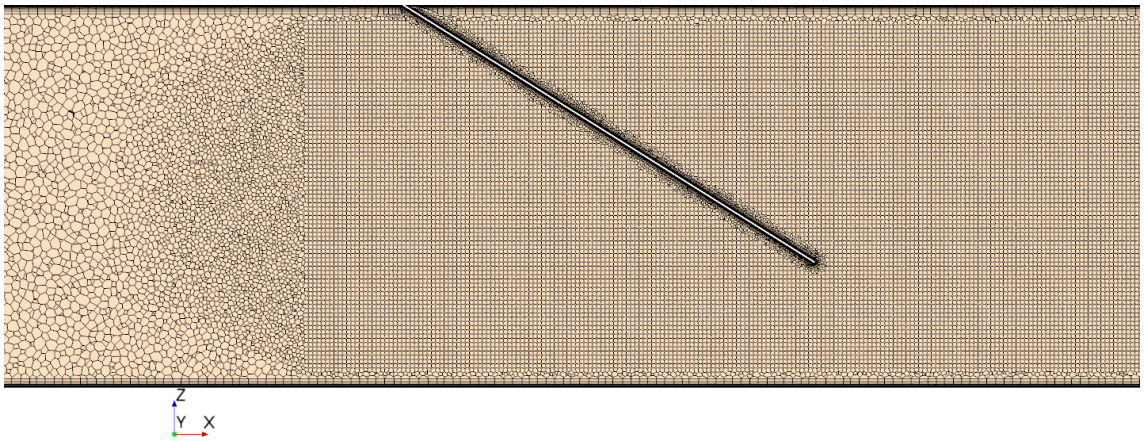

Figure 3.4: The fluid domain mesh around the thin plate, as seen in the symmetry plane of the pipe ($y = 0$). To the left a small portion of the non-refined mesh is visible. The refinement around the plate wall is apparent as well as the prism layer total thickness.

$x = 4D$, with a radius of 0.043 m[(2)]. In addition to this, a similar cylinder was introduced from $x = 15D$ to the domain end. Here, the Base size was increased to 0.0024 m. The aim of this second cylinder was to slightly reduce computational time, but still keep a domain length where boundary conditions would not affect important flow features. The volumetric controls did not affect the prism layers, which were instead refined only at the plate surfaces, in order to keep $y^+ \lesssim 1$ throughout the domain.

Special attention was paid to avoid cells with poor quality around the plate tip. Since the Advancing Layer Mesher more or less removed the low quality cells in this region it was considered well suited for the mesh construction. The final mesh consisted of 9,072,876 cells, and had some poor quality cells in the sharp corner where the plate meets the wall, see Figure A.2.

An overview of the mesh is presented in Figure 3.4, for detailed representations of different areas see Appendix A. The complete mesh settings are listed in Table A.1.

3.2.2 Boundary Conditions

For the pipe inlet, a velocity inlet boundary condition was used. To achieve a fully developed turbulent velocity profile, theory gives that the upstream length would have to be in the order of 30 pipe diameters[(3)] [6]. To reduce this length, and hence computational time, a fully developed velocity profile was computed separately and then applied at the inlet. The turbulent viscosity ratio obtained from the same separate simulation was also used at the inlet.

The computation of the velocity profile was carried out using a thin axial slice of the original duct. An interface was created between the inlet and the outlet of the slice, and a periodic boundary condition with the fully developed flow option was

[(2)]The radius was set so that the refinement would cover all of the polyhedral mesh, but not include the prism layers on the duct wall

[(3)]Based on the sixth-power-law for the entrance length $L_e = D \cdot 4.4Re^{1/6}$

chosen. In the first stiff plate simulation, the aim was to have an upstream centerline velocity of 50 m/s, as was the case for the velocity profile measurements in [2]. By iteration, it was concluded that a mass flow rate of 0.324 kg/s gave a center line velocity of 50.0 m/s, this corresponds to a mean[4] Mach number of 0.125[5]. This is slightly different compared to the experimental results in [2], where a centerline velocity of 50 m/s corresponded to a mean Mach number of 0.124. For the second simulation of the stiff plate, a mass flow rate of 0.479 kg/s gave a center line velocity of 73.4 m/s and a mean Mach number of 0.188, which was the same Mach number as was used in experiments. Otherwise the settings were chosen equal to what would be applied to the steady simulation of the complete pipe, further discussed in Section 3.2.3, with one exception: for convenience, another computational grid was used. However, a study on three different meshes showed no major differences in the resulting velocity profile, indicating that grid independence was achieved. This resulting velocity profile is shown in Figure 3.5.

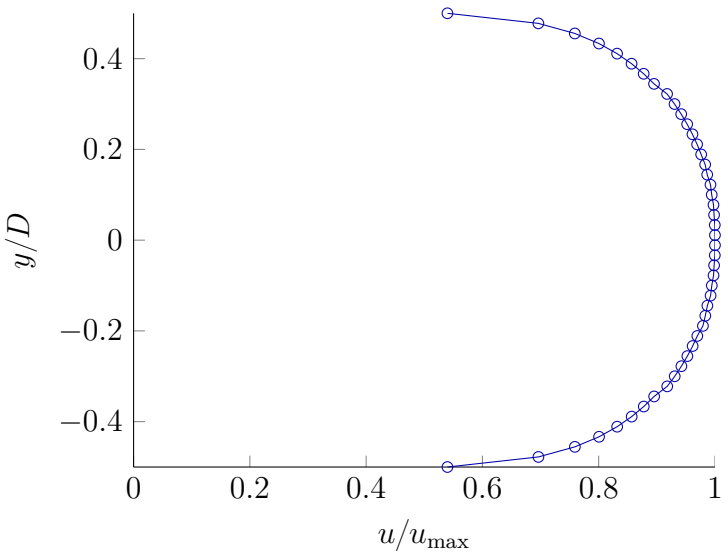

Figure 3.5: The normalized velocity profile that was specified as inlet condition. Here, the maximum velocity $u_{\max} = 50$ m/s. It should be noted that for the case with the higher velocity, $u_{\max} = 73.4$ m/s, the velocity profile is practically identical.

The pipe outlet was modelled as a pressure outlet with $p = 0$ Pa, and the pipe wall and plate surface were both modelled as walls with no-slip conditions.

3.2.3 Initial Conditions

Having set up the computational domain with the boundary conditions mentioned above, RANS in combination with the $k - \varepsilon$ turbulence model was applied. The complete settings are presented in Table B.1. The model was run until the residuals

[4] Here corresponding to a spatial mean, sometimes denoted bulk.

[5] Throughout the report, the speed of sound $a = 340$ m/s. Furthermore, M was based on a mean velocity of $u_{\text{mean}} = 42.5$ m/s computed from the mass flow rate above.

were low and steady, and thus the simulation considered converged[6]. The resulting solution was used as initial conditions for the transient simulations.

3.2.4 Transient Solver Settings

Detached Eddy Simulation (DES) was selected together with Spalart-Allmaras[7] as the turbulence model[8] for the transient simulation. Additional settings for this physics model are collected in Table B.2.

A time step of $\Delta t = 5 \cdot 10^{-5}$ s was chosen. This time step was based on the fact that wishing to reproduce results from [2], frequencies up to 1,000 Hz needed to be resolved. This corresponds to a period time of 0.001 s, and 20 steps per period was recommended to properly resolve this frequency [11]. In addition 10 and 15 inner iterations per time step were used for the lower and higher velocity case respectively. With these settings, the continuity residual dropped one order of magnitude within each time step. Furthermore, controls of pressure and velocity were performed for some points in the domain to assure that the values stabilized within the time step.

The transient simulations for the stiff plate were started from the initial conditions described in Section 3.2.3. The settings used for the solver are listed in Table B.5. A total of 2 s of flow was simulated. The first half second of the simulation time was considered undeveloped and was hence not included in the post-processing.

3.3 Modelling of Plate

In the rigid plate case, the plate was assumed to be infinitely stiff, and hence no modelling of the plate was needed. Since experiments show that the vibrations of a 3 mm plate in this case are of such a small magnitude compared to the thickness, this should be a valid approximation [2].

The flexible plate, with a thickness of 0.5 mm, on the other hand was modelled using the predefined Star CCM+ material Carbon Steel UNSG101000 ($\rho = 7832$ kg/m^3, $\nu = 0.285$, $E = 200,000$ MPa). The motion of the plate was computed using the built-in solid stress FE model, for complete settings see Table B.4.

The part of the plate boundary coinciding with the duct wall was assigned a fully restrained boundary condition.

3.3.1 Computational Mesh

The solid mesh was created using the Tetrahedral Mesher with the Surface Remesher and, since the plate is indeed thin, the Thin Mesher. A Base size of 0.01 m was chosen, which is substantially larger than for the surrounding fluid mesh. Mid-side vertices were added to reduce the stiffness, resulting in second order triangular prism elements, also called *Wedge15* elements. Additional settings are listed in Table A.2.

[6] A total of 1,500 iterations were required

[7] This default Star CCM+ setting implements a variation of DES known as Improved Delayed Detached Eddy Simulation (IDDES)

[8] With an estimated $Re \approx 87,000$, the flow is clearly turbulent and thus the turbulence has to be considered

Using two thin layers resulted in a mesh of 20,811 cells. An overview of the mesh is presented in Figure 3.6, and a zoomed in view is presented in Figure A.3.

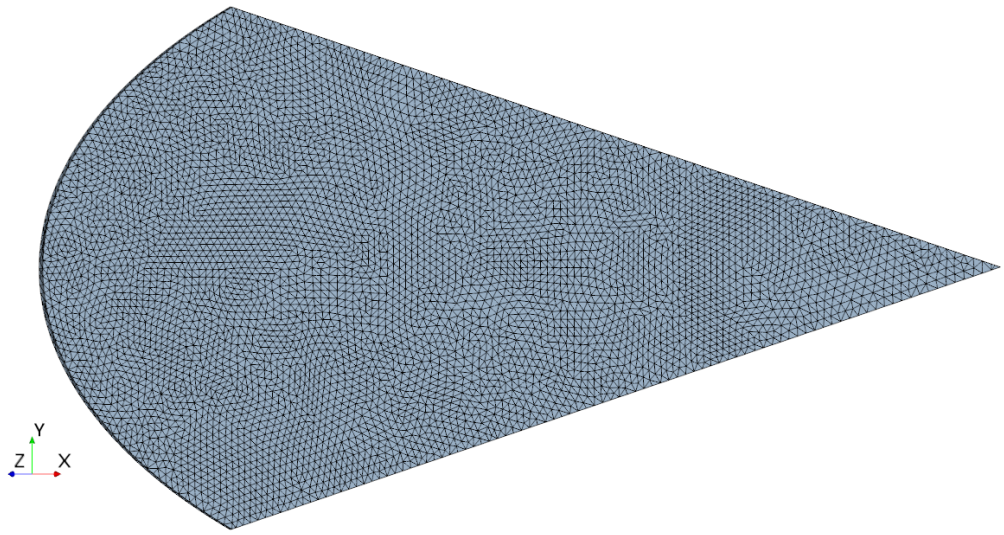

Figure 3.6: The mesh used for the thin solid plate. The plate has the same orientation as in Figure 3.2.

A mesh indepency study for the plate was carried out, where a static FSI simulation was performed for three different meshes, see Table 3.1, and the displacement of the plate tip was measured. No significant change in static deflection was observed when using the finer meshes. Furthermore, it was confirmed that the recommendation of a cell aspect ratio smaller than 5 was satisfied [11].

Table 3.1: The different meshes investigated in the plate mesh independency study.

No. elements	No. thin layers	Base size
~ 21000	2	0.01 m
~ 85000	3	0.006 m
~ 240000	4	0.004 m

3.3.2 Modal Analysis

To verify the Star CCM+ model of the plate, a simple modal analysis was performed on the thin plate to find the eigenfrequencies of the model. Since Star CCM+ does not have any native modal analysis functionality, the following strategy was used: a model of only the plate, with the same computational mesh and clamped edge boundary condition that would be used in the fluid-structure problem, was set up. A small, constant surface load[(9)] was applied to the free surfaces of the plate for a brief period of time, creating an oscillating motion. When the oscillating plate was close to an undeflected state, the load was removed, allowing the now excited plate to vibrate freely. By releasing the plate at this specific moment, it went

[(9)] Star CCM+ does not support point loads.

into a multi-modal vibration state allowing examination of the first three modes. To find the bending modes, the displacement of the tip of the plate was tracked. The modal vibrations were monitored for 0.047 s, a time which spanned 4 periods of the dominating mode. Analysis of the movement was performed using the FFT function in MATLAB.

In order to find the torsional modes, two equal loads with opposite direction were applied; positive for $y < 0$ and negative otherwise, where y is defined as in Figure 3.2. The motion was tracked via a point at the plate edge. Otherwise the procedure was as before. The plate modal vibrations were monitored for 0.048 s and this included 24 periods of the dominating frequency. The placement of the measuring probes is visualized in Figure 3.7.

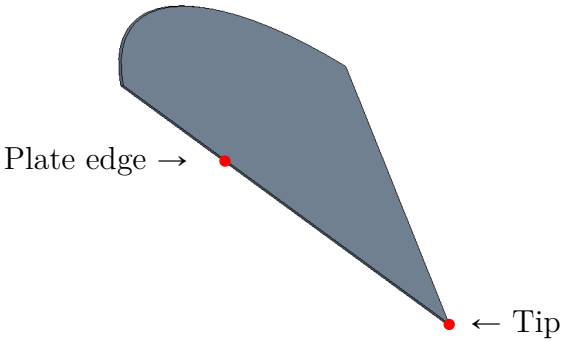

Figure 3.7: The placement of the two probes used to capture the plate displacement for the modal analysis.

3.4 Fluid-Structure Interaction

The fluid-structure interaction simulation was set up using the same settings used for the previous fluid and solid simulations respectively, as far as this was possible. The lower velocity of $M = 0.125$ was simulated. The meshes were created as described in Sections 3.2.1 and 3.3.1, resulting in a total of 9,089,780 cells[(10)]. As opposed to the stiff plate case, the meshes were now allowed to deform. The motion specification was set to Morphing for the fluid mesh and Solid Displacement for the solid mesh. The physics models were also kept the same, as well as the boundary conditions, with the exception of the regions where the plate and the flow coincide, which were now treated as interfaces.

3.4.1 Fluid-Structure Interface

For each surface where the fluid and the solid domain are in contact, a *Mapped contact interface* was created. This allows for the meshes of the respective domains to be non-conformal, enabling them to be of different type and resolution. Instead of

[(10)] 9,069,133 cells for the fluid domain and 20,647 cells for the solid domain

having a direct vertex to vertex match, which would have been difficult to implement due to the different requirements on the fluid and the solid mesh respectively, the data is interpolated from one mesh to the other. At the fluid boundary included in each interface, the Morpher option was set to Floating, and at the corresponding solid boundaries the option Solid Displacement was chosen.

3.4.2 Initial Conditions

To find suitable initial conditions for the transient FSI simulation, a static simulation was performed. In this simulation, the fluid domain was treated as in Section 3.2.3, while for the solid domain a steady solid stress model was used (see Table B.3). Only one non-default solver setting was used: Morph From Zero was enabled, meaning that when morphing, the mesh was recalculated from its original state instead of from the previous mesh solution. The unchanged settings imply that a two way coupled solver was used: the fluid domain was solved using RANS, and that the plate was allowed to deflect due to the fluid forces of the steady simulation. Since the fluid forces were steady, the plate obtained a constant deflection. As before, the static simulation was run until the residuals were low and steady[(11)], and the resulting solution was then used as initial conditions for the transient simulation.

3.4.3 Transient Solver Settings

Changing the physics models of the FSI simulation to DES for the fluid domain and transient solid stress for the solid resulted in additional solver settings. Since the simulations are of a low density fluid around a high density solid, a loosely coupled FSI model was considered sufficient. To implement this, the FSI Displacement Convergence Tolerance was changed to 1, meaning that data was only transferred once per time step. Surveying the residuals, and using the same criterion as in Section 3.2.4, a number of 12 inner iterations was chosen. The complete transient solver settings are presented in Table B.6. In conformity with the stiff plate case, a total of 2 s were simulated and the first 0.5 s was disregarded in the post-processing.

3.5 Post-processing

When it was convenient, post-processing was performed directly in Star CCM+. Otherwise, Matlab was used. Some information regarding the procedures is given below.

3.5.1 Velocity Profiles

To find velocity profiles downstream of the plate, both space and time averaging were used. The velocity magnitude of the flow was saved at 21 by 21 equally spaced monitor points spanning the whole diameter of the duct, see Figure 3.8. In the

[(11)] 1,500 iterations was found sufficient

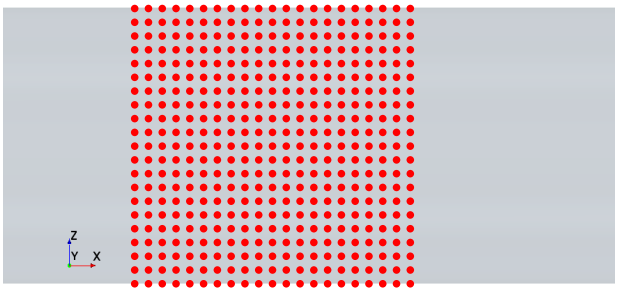

Figure 3.8: The grid of probe points used for computation of velocity profiles. The figure shows the grid used for extraction of a profile in the z-direction, meaning that the domain is viewed as in Figure 3.1. This also means that $y = 0$ for all points.

streamwise direction, the points covered $0.5D$ upstream and downstream respectively of the coordinate investigated. A total of 200 samples were collected, spanning a time of 0.1 s. The velocity was then averaged with respect to time and streamwise direction.

3.5.2 Sound Estimation

To find the generated sound, the pressure average was computed in planes perpendicular to the flow direction. This was done for every time step and for a number of cross sections both upstream and downstream of the plate. By inspecting the pressure drop around the plate and observing where the pressure had recovered, it was concluded that planes located at $-2D$ upstreams and $5D$ downstreams of the plate were suitable for sound estimation. This will be developed further in Section 4.3.

The sound estimation procedure started by computing the difference between upstream and downstream pressure average for every time step. The mean of the resulting time signal was subtracted, to center the signal around zero. Then the PSD of the signal was computed using the Welch method[(12)] and applying a Hanning window. To achieve correct input data for the method, the signal was divided into several shorter subintervals, all with a length of 2048 (2^{11}) samples, and every subinterval had a 50% overlap with the next. This results in a total of approximately 28 subintervals.

Since the obtained autospectrum is equivalent to the averaged squared Fourier transform of the pressure fluctuation, it can then be expressed in dB/Hz using Equation 2.8. The MATLAB code used can be found in Appendix D.

3.5.3 Investigation of the Flow Physics

To better understand different flow features, contour plots of pressure and velocity in the symmetry plane (where $y = 0$) were sampled. Furthermore, pairs of probe points were placed behind the plate edge. Three pairs of points at varying height and separated by varying horizontal distances were used. In addition, a single point was added behind the plate tip. The locations of the points are visualized in Figure 3.9.

[(12)] The MATLAB function `pwelch`

The instantaneous pressure in each of the points was sampled, such that the auto- and cross-spectral densities[13] of the fluctuations could be investigated. From this the coherence, γ_{xy}^2, could be computed according to Equation 2.23. From the real and the imaginary parts of the cross-spectral density the phase shift between the monitor pairs could be found[14].

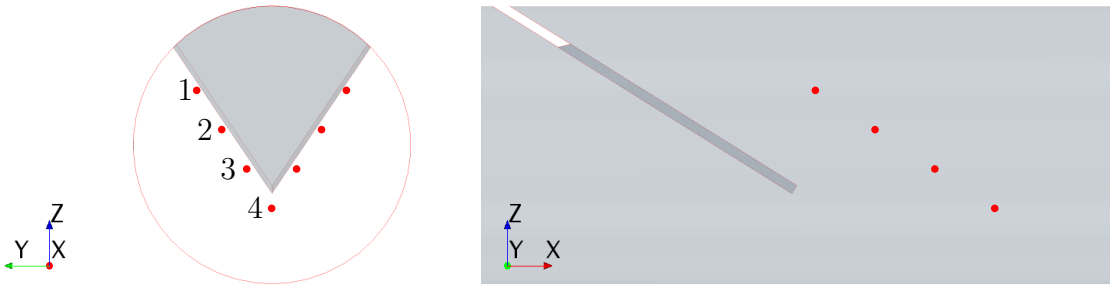

Figure 3.9: The placement of the seven probes used to investigate instantaneous pressure variations around the plate, seen from two different perspectives. Note that the two subfigures have the same scale. The graphics were taken from the stiff plate model, where the plate is represented by void, which explains the dent in the side view.

The resulting coherence and phase shift data was studied using a location dependent version of the Strouhal number. The characteristic length was given by the width of the plate at the same height as the corresponding probe pair. The characteristic velocity was given by the inlet velocity, see Figure 3.5, at the $y-z$-coordinate of the points. The values are presented in Table 3.2.

Table 3.2: Quantities used to calculate the alternative Strouhal number, St_{var}. The plate width was used as characteristic length and the upstream local velocity as characteristic velocity.

Point pair	Width (ℓ) [m]	Velocity (u) [m/s]
1	0.044	45.0
2	0.027	48.8
3	0.010	49.6

[13] The cross power spectral density was computed using the MATLAB function `cpsd`, which like `pwelch` employs the Welch method

[14] Using the cross-spectral density as input argument to the MATLAB function `angle`

4

Results and Discussion

In this chapter, the outcome of the simulations is presented and discussed. First, some results concerning validation of the numerical model (modal analysis and velocity profiles) are presented. Then, the focus is moved to sound generation. The stiff and flexible plate cases are compared. As far as possible, comparisons with experimental results from [1, 2, 3] are also performed. Thereafter some analysis of the physics in the problem (pressure and velocity) is made. Finally, some more general discussion treating error sources such as mesh quality, FSI solver performance and suitability of sound estimation method is included.

4.1 Modal Analysis

The results of the initial modal analysis of the flexible steel plate are presented in Table 4.1. Frequencies are given in terms of the Helmholtz number[(1)], which was computed using half of the maximum plate width as the characteristic length (i.e. $\ell = 0.032$ m).

Table 4.1: The result of the modal analysis. The reference frequencies are from [2], where the third column lists the experimental bending modes, and the last column lists frequencies determined with a commercial finite element software.

Mode	Freq. (He)	Ref. exp. freq. (He)	Ref. FE freq. (He)
1st bending	0.05	0.06	0.05
2nd bending	0.21	0.22	0.20
3rd bending	0.46	0.46	0.46
1st torsional	0.30	-	0.28
2nd torsional	0.74	-	0.69

As can be seen, the three bending modes found in Star CCM+ are in good agreement with both the experimentally and numerically found reference values. This indicates that the model behaves as desired. For the torsional modes, the computed eigenfrequencies differed by approximately 7% compared to the reference values. However, the reference values for the torsional modes have been computed using an FE model and there are no experimental results available for comparison.

The fact that the simulated bending modes are in agreement with the experimental ones is quite promising; if incorrect material properties had been used this would

[(1)] Helmholtz number $He = \dfrac{2\pi f \ell}{a}$.

have affected the characteristic frequencies, making them distinctly different from the experimental results. The same would be true for a too stiff FE model, however since a mesh independency study was performed for the plate, see Section 3.3.1, it is unlikely that this is the case. Therefore it seems probable that the material properties used is representative of reality.

In addition to the eigenmodes, the plate deflection could be used to confirm the plate model. However, the only experimental data available for comparison is dependent on the surrounding flow. Thus, validation of the amplitude could not be performed within the modal analysis, and will instead be discussed in connection with the drag coefficient in Section 4.3.1.

4.2 Velocity Profiles

The velocity profile used as inlet boundary condition was first presented in Section 3.2.2. To confirm its accuracy, Figure 4.1 shows the profile compared to a velocity profile measured at $x = -3D$. The two profiles are indeed in very good agreement.

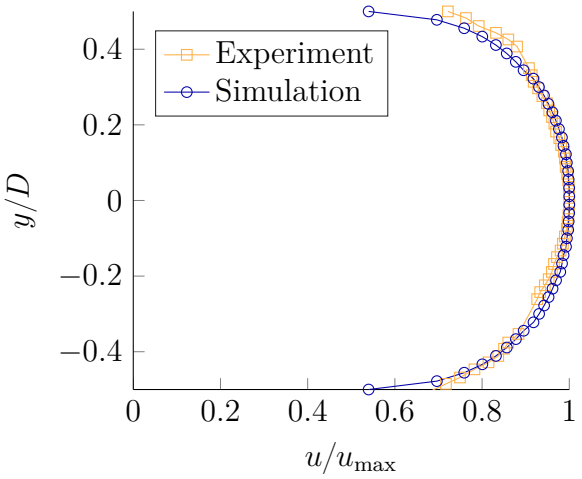

Figure 4.1: The normalized inlet velocity profile, also shown in Figure 3.5, together with experimental data from [2]. Both cases have an upstream centerline velocity of 50 m/s.

The downstream velocity profiles were calculated according to the description in Section 3.5.1 at $3D$, $6D$ and $9D$ downstream of the plate. Measurements were taken along both the y and z axes. The results for the stiff and the flexible plate, together with the experimental results of [2], are shown in Figure 4.2 and 4.3 respectively. Both simulations and experiments have an upstream centerline velocity of 50 m/s.

Note that for all velocity profiles, the experimental data has been extracted manually from Figure 5 and 6 of [2]. The extracted data has been renormalized to enhance comparability with the simulation data. This means that the experimental data in Figure 4.2 and 4.3 is an approximation. Since it is only used for visual comparison, however, the effect of this should be negligible.

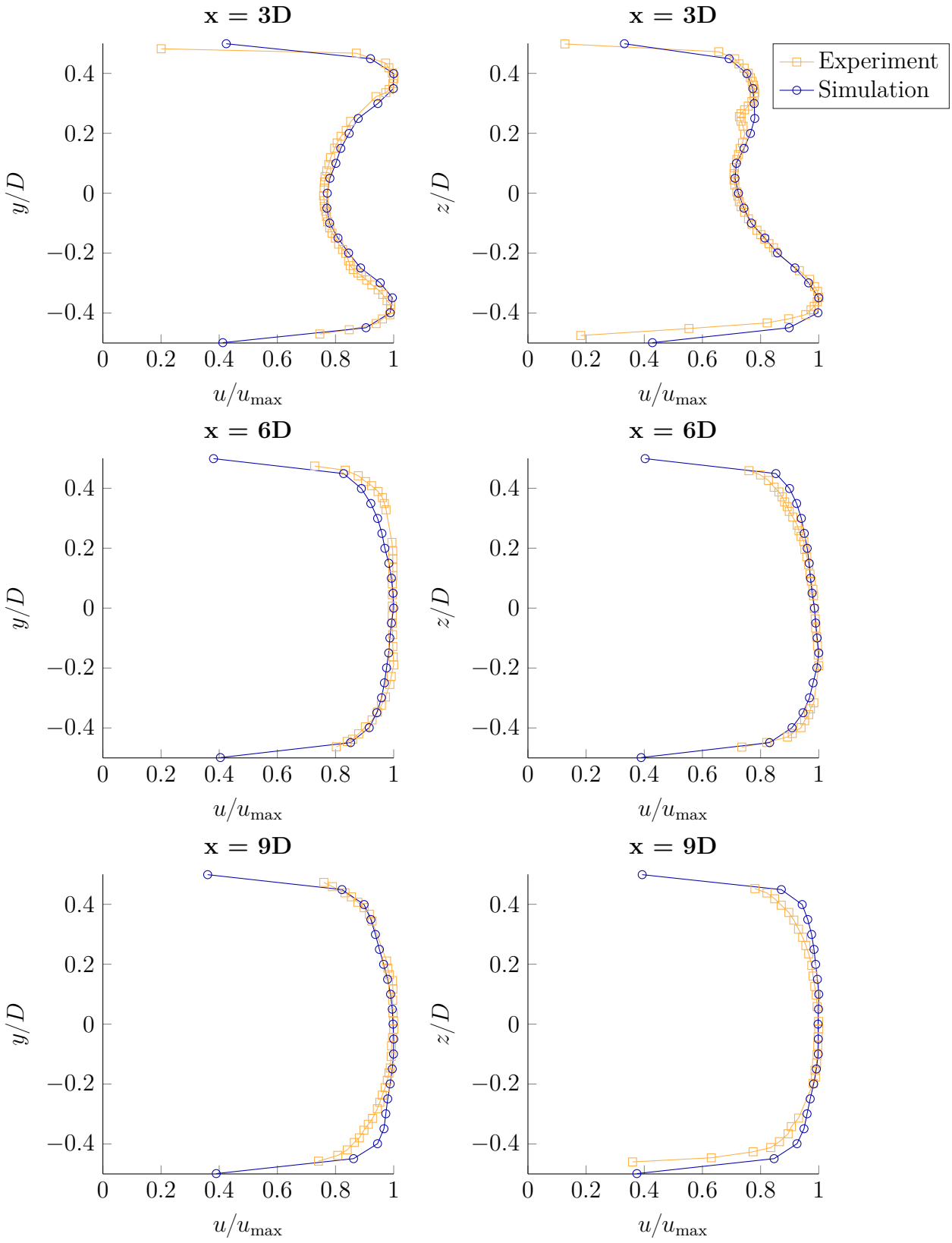

Figure 4.2: The normalized velocity profiles obtained from the stiff plate simulation together with experimental data from [2]. Both cases have an upstream centerline velocity of 50 m/s. The legend is common for all plots.

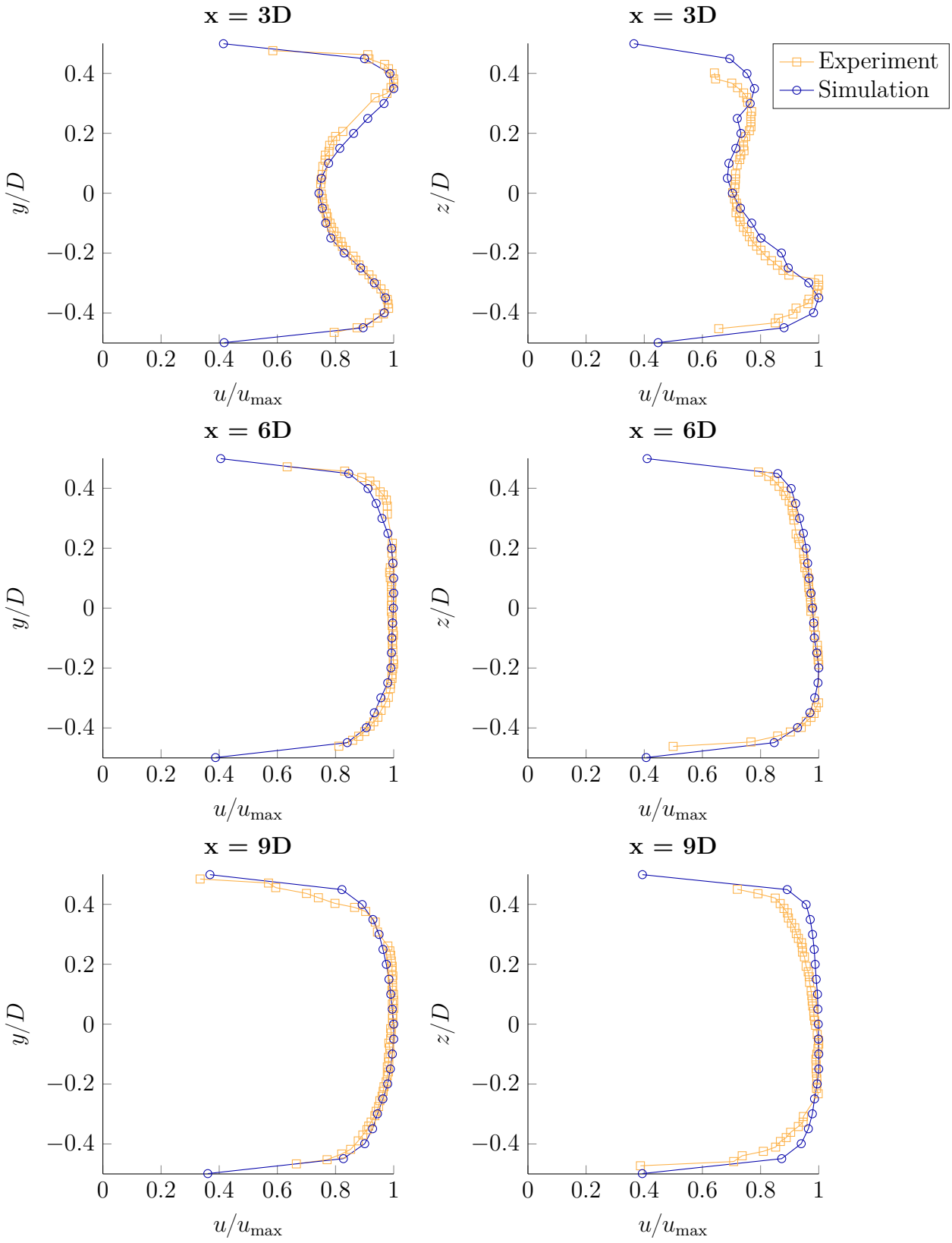

Figure 4.3: The normalized velocity profiles obtained from the flexible plate simulation together with experimental data from [2]. Both cases have an upstream centerline velocity of 50 m/s. The legend is common for all plots.

From Figure 4.2, it seems that in the stiff plate case, close to the plate, the velocity profiles of the simulation correspond very well to the experiment. This is promising since the plate is important for the sound and hence accurate physics close to the plate is required.

Further downstream (at $x = 6D$ and $x = 9D$), the simulated profiles are less rounded than the experimental ones, meaning that the simulated velocity close to the wall is higher than in the experiments. The more square velocity profiles indicate that the amount of turbulence in the flow may be larger in the simulation. This means that the turbulence is not decaying as quickly as in experiment, probably due to imperfection in the wall treatment. An investigation of the turbulent kinetic energy could give increased insight into this, but falls outside the scope of this thesis.

Supposedly the velocity profiles will become more similar further downstream. Considering that the inlet velocity profile was created with the same settings and yielded an accurate fully developed velocity profile, the downstream velocity profiles should approach the experimental ones, as the flow once again approaches a fully developed state.

Another interesting observation is that the velocity profile in the y-direction at $x = 9D$ is slightly asymmetric, which is not expected. It is possible that sampling the velocity over a longer time span would remedy this problem.

For the flexible plate, Figure 4.3, similar trends can be observed: close to the plate the profiles coincide well, while further away ($x = 9D$) the simulated profile becomes slightly too square. However, the velocity profile in the z-direction at $x = 3D$ does not match the experimental one perfectly; the experimental velocity profile has its maxima slightly closer to the center of the duct, and shows a more rapid decrease in velocity as z/D approaches 0.5 than any other profile. It is possible that the difference is due to some problem in the simulation, however there is also a risk that the experimental measurements are not as accurate as desired.

Due to the data available, the velocity profile validation can only be performed for the lower velocity case.

4.3 Pressure Recovery

The plate causes a drop in the pressure in the pipe. Measurements of the average pressure in cross sections of the pipe at different x-locations allows for investigation of the pressure drop caused by the plate. Figures 4.4a and 4.4b show the average pressure as a function of the position in the streamwise direction for the stiff and the flexible plate respectively. In addition to averaging the pressure over the cross section, a time average over a time of 0.5 s has been performed.

From Figure 4.4, it is clear that there is a large pressure drop at the location of the plate. Further downstream the pressure recovers although it does not reach the upstream pressure level. Before and after the plate, there is a linear pressure decrease due to friction between the fluid and the pipe wall. This decrease can be compensated for to obtain the pressure drop caused by the plate. In Figures 4.4c and 4.4d, the linearly decreasing pressure component has been subtracted. Note that the pressure curve has also been translated such that the outlet boundary

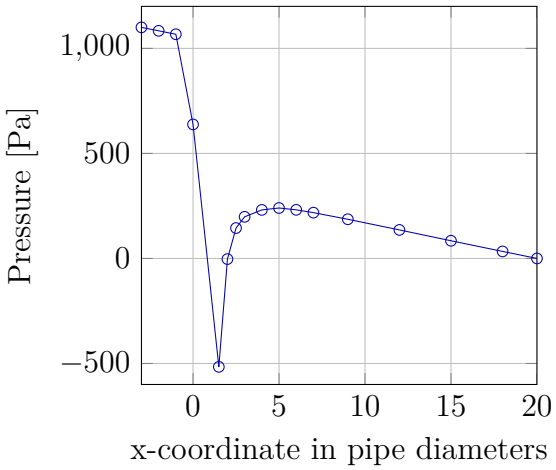

(a) Pressure recovery for stiff plate including friction loss due to walls.

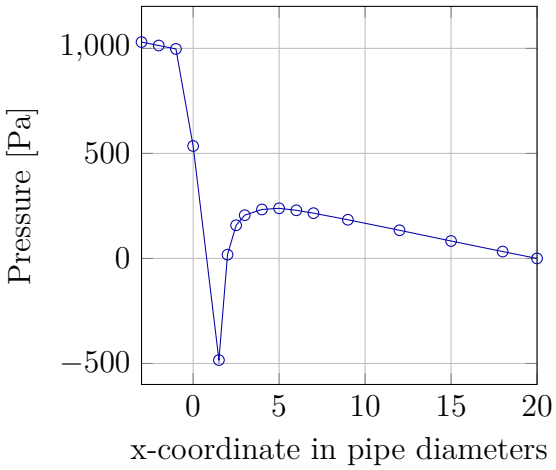

(b) Pressure recovery for flexible plate including friction loss due to walls.

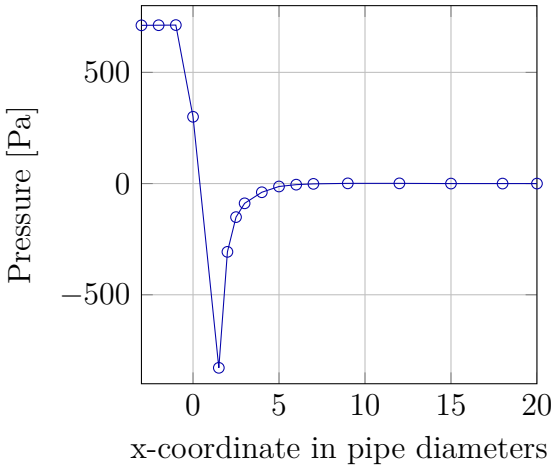

(c) Pressure recovery for stiff plate when friction loss has been corrected for.

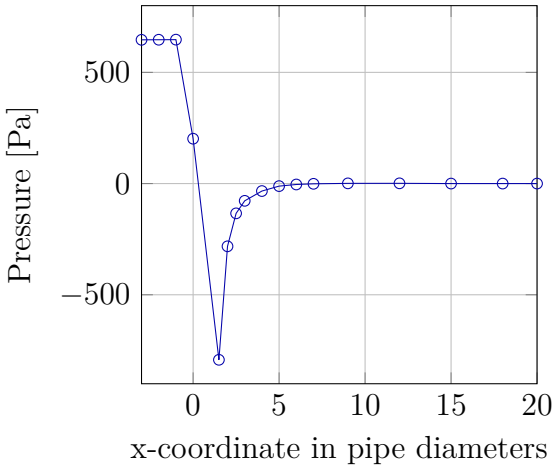

(d) Pressure recovery for flexible plate when friction loss has been corrected for.

Figure 4.4: Pressure recovery in the duct with and without friction loss. The pressure is spatially averaged over the pipe cross section and since the pressure is fluctuating a time average over 0.5 s is also performed. The point at $20D$ was added manually, since the pressure here is known from the outlet boundary condition.

condition is still fulfilled. Studying the pressure drop, it seems that the pressure can be considered recovered at $x = 5D$.

The fact that the pressure, when friction is disregarded, is constant both before and after the pressure drop indicates that sufficient upstream and downstream pipe length has been included to capture the effect of the plate. It also confirms that the friction loss due to the duct walls is linear, as expected.

4.3.1 Drag Coefficient

Using Figures 4.4c and 4.4d, the pressure loss solely due to the presence of the plate can be found. From this pressure loss, the drag coefficient C_D can be computed ac-

cording to Equation 2.3 for both the experiments and the simulations[(2)]. The values are computed for the mean velocity 42.5 m/s, for which there are also experimental values to compare to. Resulting values are presented in Table 4.2, along with experimental data from [1]. The experimental procedure included measurements of pressure loss in an empty duct and in the duct with the plate, for different velocities. This data was post-processed to find the pressure loss due to the plate; see Appendix C for details.

Table 4.2: Values for the pressure loss in the pipe for simulation and experiment. Three different aspects of the pressure loss are given: pressure loss per meter due to wall friction in an empty pipe, pressure loss due to the plate (when the effect of wall friction has been corrected for) and drag force based on the plate pressure loss.

Plate	Source	$\frac{\Delta p_{\text{empty}}}{\Delta L}$ [Pa/m]	Δp_{plate} [Pa]	C_D
Stiff	Simulation	187	711	2.01
	Experiment	202	629	1.76
Flexible	Simulation	186	646	1.83
	Experiment	202	549	1.54

It can be concluded that the drag coefficient for the flexible plate is lower than for the stiff plate for both simulation and experiment. The main reason for this is probably that the flexible plate is deflected, meaning that the actual projected area is decreased. However, since this is not considered in the calculations of the projected area, a lower value of C_D is expected.

It is also clear that there is a difference in the predicted drag compared to experiments. This is a consequence of the difference in pressure drop over the plate, which seems to be overpredicted in the simulations. This could be a result of the different methods used to find the pressure loss due to friction. The pressure loss per unit length due to friction in the empty pipe appears to be slightly underpredicted by simulations. If the pressure loss in the empty pipe is assumed to be the same as in the experiment, the predicted pressure drop caused by the plate is almost 6% lower, resulting in a corresponding decrease of C_D. However since the experimental friction pressure loss $\frac{\Delta p_{\text{empty}}}{\Delta L}$ is computed using a friction factor that would not be representative of the simulation model, this method is rejected.

The fact that the predicted pressure loss due to friction in the pipe is too low indicates once again that the wall treatment might not be entirely correct. That the pressure drop over the plate is too high is harder to explain. Possibly, a better wall treatment would improve this too, but there is also a risk that an increase in friction would contribute to an even higher Δp_{plate}.

The deflection of the plate is never stated explicitly in [1] or [2], but the drag coefficient can also be used to analyze the deflection of the flexible plate. Introducing a flexible plate leads to a decrease in C_D of 12.5% in the experiments, and to a decrease of 9% in the simulations. Since the drag coefficient decreases more for experiments it is reasonable to think that the deflection is underpredicted by the FSI simulation.

[(2)] Calculations of and values of constants can be found in Appendix C.2

4.4 Flow Induced Plate Vibrations

For the modal analysis presented in Section 4.1, the flexible plate was excited by an applied body load and allowed to vibrate freely, unaffected by other forces: a situation comparable to vacuum. In the FSI simulation on the other hand the plate is excited by the surrounding air, which can also dampen the induced vibrations. This might affect the behaviour of the plate.

Studying the displacement of the plate tip, see Figure 4.5, there is an obvious variation of amplitudes present. Large amplitudes appear to correspond to a specific frequency, while for small amplitudes it is obvious that other, higher, frequencies are also present. Note that the amplitude of the oscillations keeps varying in the same way as visualised in Figure 4.5 during all of the time simulated. Also note that no pattern regarding the shift from small to high amplitudes or vice versa was observed.

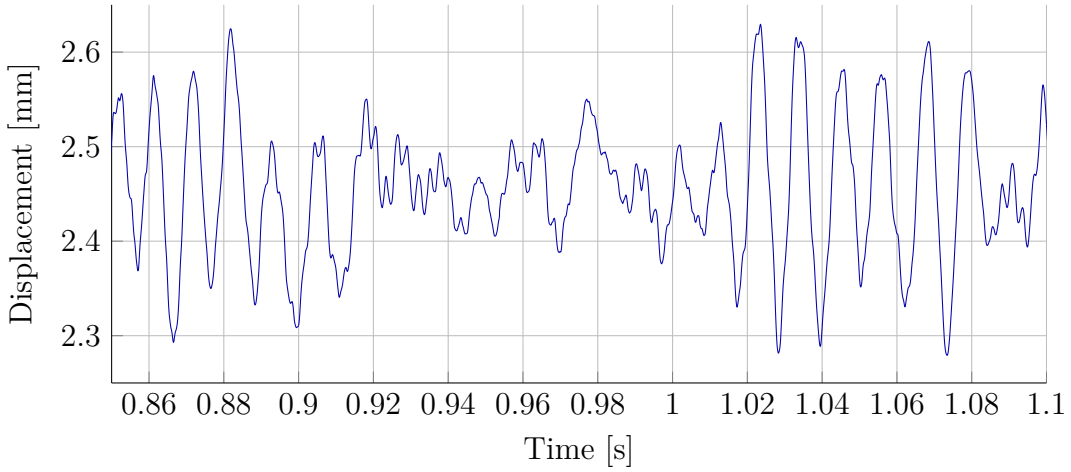

Figure 4.5: The displacement of the tip of the plate for a short period of time, chosen to show the great variation in amplitude present. The pattern of irregular changes in amplitude continues troughout the simulation.

In the same way as for the modal analysis, the frequencies with which the plate vibrates is computed. The frequencies are compared to experimental reference frequencies in Table 4.3[(3)]. The eigenfrequencies still seem to coincide well with the experimentally found bending modes, which indicates that the flow will cause the plate to vibrate at its eigenfrequencies. Since the deflection of the plate tip, which is located at the plate symmetry line, was used for analysis, possible torsional modes could not be found.

The displacement can also be analyzed with respect to extrema, mean and amplitude, see Table 4.4. In [2] it is estimated that the oscillations have a magnitude of approximately 0.4 mm. In Table 4.4 the maximum amplitude is presented. Given the variation in amplitude it is clear that the mean amplitude is smaller than 0.53 mm,

[(3)]This table can also be compared to Table 4.1, which lists the eigenmodes from the modal analysis

Table 4.3: The vibration frequencies of the plate. Experimental reference frequencies from [2].

	Frequency (He)	Ref. frequency (He)
1st bending	0.05	0.06
2nd bending	0.21	0.22
3rd bending	0.50	0.46

and probably not too far from 0.4 mm. This suggests that the simulation quite accuratley predicts the amplitude of the vibrations.

Table 4.4: The mean, maximum and minimum displacement of the plate tip, and the consequent maximum amplitude of vibrations. All values are given in mm.

Mean	Max	Min	Amplitude
2.46	2.72	2.19	0.53

As mentioned in Section 4.3.1 the plate tip displacement was not explicitly stated in any of the experimental studies, but the drag coefficient analysis indicated that the deflection was too small for the simulations. In Figure 9 of [2], an image of the plate in an undeflected and a deflected state is shown. From this a crude estimate of the tip displacement was found to be around 3 mm. This confirms that the simulated deflection of approximatly 2.46 mm is probably somewhat too small.

4.5 Sound Generation

In Figure 4.6, the sound spectrum for the stiff and flexible plate respectively is presented and compared to experimental values from [3]. The frequency is given in terms of the Strouhal number[(4)], which is computed using the same characteristic length as for the Helmholtz number ($\ell = 0.032$ m) together with the mean velocity. For the simulations the velocity is computed from the mass flow rate, giving $u_{\text{mean}} = 42.5$ m/s, while for the experiments, the mean velocity is obtained by scaling the centerline velocity (52 m/s) by a constant factor of 0.82 [1]. The difference in frequency resolution between the simulations and the experimental measurements is a result of the difference in signal length: in the experimental case, a signal of around 10 s was available whereas in the simulation, the signal analyzed spans 1.5 s.

From Figure 4.6a it can be noted that the sound estimate from the simulation of the stiff plate corresponds well to the experimental measurements regarding level. The experimental maximum at $St \approx 1.2$ is also fairly well predicted by the simulation, although it is somewhat overpredicted and has its peak at the slightly higher frequency of $St = 1.3$.

Moving on the the flexible plate in Figure 4.6b, it is remarkable that the clear dip in sound around $St \approx 1.9$ is not captured by the simulation. Instead there seems to be a peak in the sound spectrum at this frequency, resulting in a significantly

[(4)]Strouhal number $St = \dfrac{2\pi f \ell}{u}$

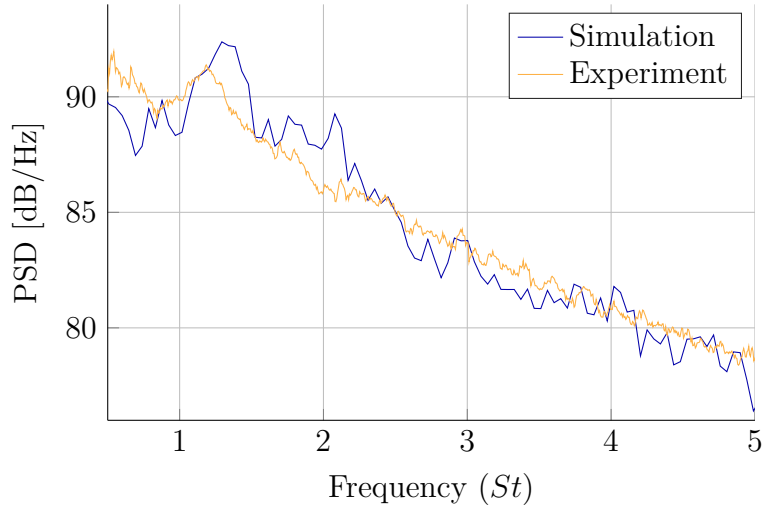

(a) Stiff plate

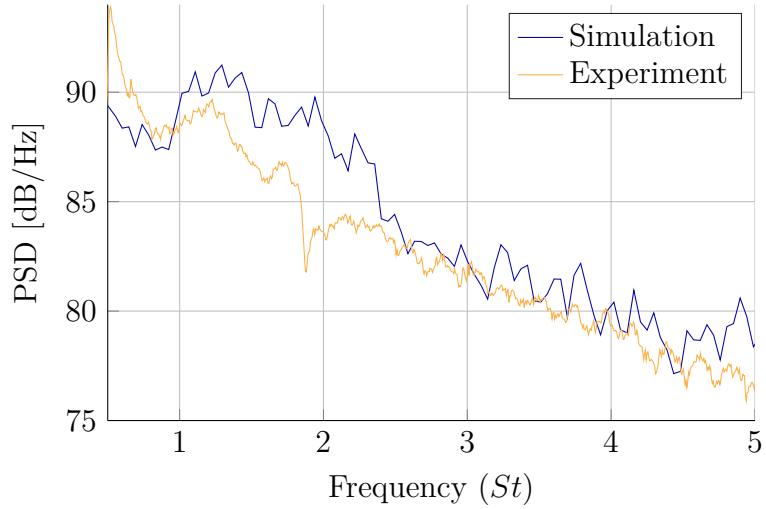

(b) Flexible plate

Figure 4.6: The PSD sound estimate as a function of the frequency for $M = 0.125$. The experimental result is given by the sum of the upstream and downstream components, $G^s_{11} + G^s_{22}$, from [3]. Frequency resolution for the simulation is 9.77 Hz.

different level between the cases. For higher frequencies ($St \geqslant 2.5$) the levels coincide better. The peak at $St = 1.2$ is fairly well predicted, although once again slightly overpredicted and with a minor shift in frequency.

The fact that the mechanism behind the reduction of sound at $St \approx 1.9$ is unknown makes it difficult to speculate about the reasons behind the absence of a dip in the simulation result. It could be due to a problem in the simulation set-up, but it could also be caused by some shortcoming of the numerical solver, or an inability in the sound estimation method to capture this specific phenomenon. The error sources will be discussed continuosly in the remainder of the chapter.

To evaluate whether the flexible plate reduced the sound compared to the stiff plate, the spectra from both simulations are presented together in Figure 4.7. The difference between the two cases is much smaller than expected. The experimental

results show that the sound level is generally 1-2 dB lower for the flexible case. This difference might be explained by the deflection of the plate, decreasing the size of the intruding object when projected in the streamwise direction. The fact that the difference is not larger between the simulation cases indicates, once more, that the deflection is too small.

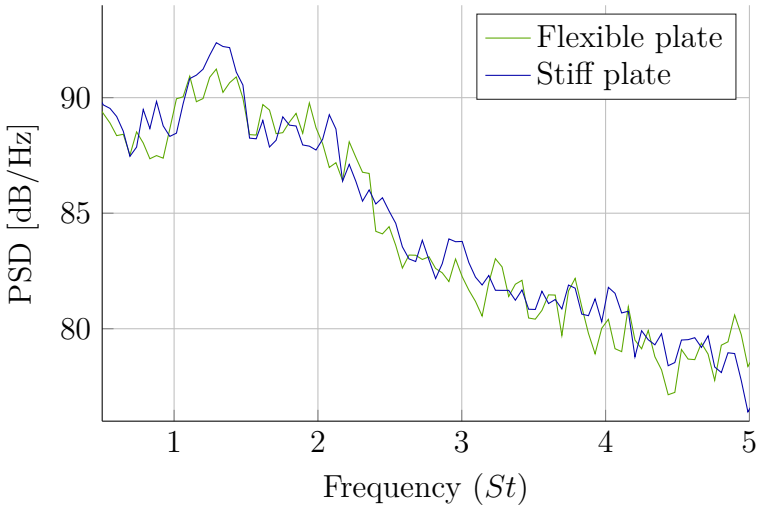

Figure 4.7: The PSD sound estimate as a function of frequency, for the stiff and flexible plate simulations, $M = 0.125$. The frequency resolution is 9.77 Hz.

4.5.1 Sensitivity to Downstream Measurement Location

As a complement to Figure 4.6, Figure 4.8 shows sound spectra computed from a number of different downstream cross sections together with experimental data for the stiff plate. From this, it is obvious that choosing the correct location for the measurement is essential. The same trend of decreasing levels are present in the FSI simulation, with the addition that around $St = 5$, the level of sound estimated close to the outlet climbed in dB, approaching the levels measured close to the plate; the reason for this is still unclear.

As mentioned in Section 2.4.4, the wave propagation speed in an incompressible flow simulation can be assumed to be infinite. Accordingly, the sound estimation was expected to give the same result independently of the upstream and downstream pressure measurement location chosen, as long as the measurements are taken outside of the pressure drop region. As mentioned earlier, it can be concluded from Figure 4.4 that the drastic drop in pressure caused by the plate has recovered at $x = 5D$. Therefore it is assumed that the pressure drop induced by the plate is not the only factor affecting the sound level.

It is clear that the further downstream of the plate the measurement plane is placed, the lower the sound level. From $x = 5D$ to $x = 9D$, there is a difference of approximately 6 dB. As the distance from the plate increases, the difference in levels between computed sound spectra decreases; it was noted that for $12D$, $15D$ and $18D$ the sound curves coincide. However with the outlet located at $20D$, it cannot be ruled out that the decreasing difference in sound level is a boundary effect.

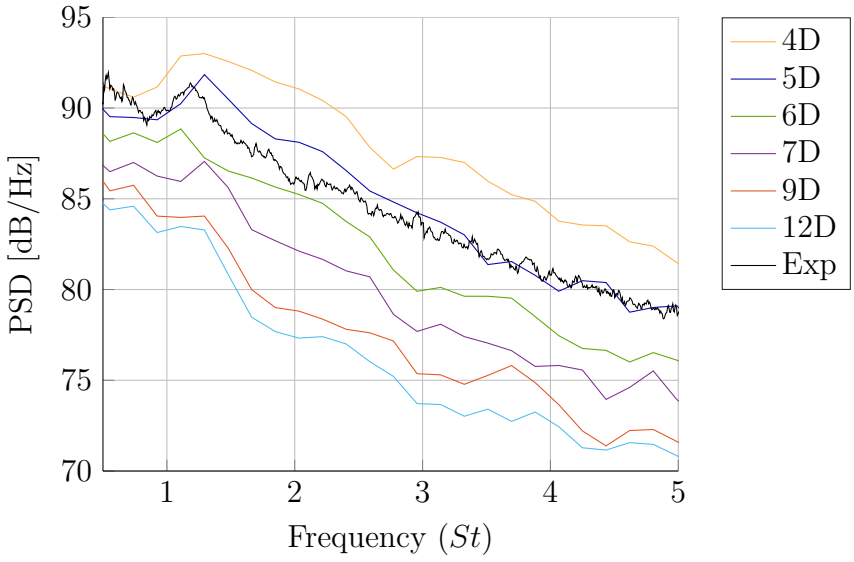

Figure 4.8: The PSD sound estimate for the stiff plate, $M = 0.125$, for different downstream measurement locations. Upstream measurements were taken at $x = -2D$. A low frequency resolution (39 Hz) was chosen for the simulation, to emphasize level difference. The experimental result is the sum of the upstream and downstream component, $G^s_{11} + G^s_{22}$.

The decreasing sound levels cannot be explained by the friction loss in the duct. The friction loss only affects the mean pressure, and in the sound estimation the mean is subtracted, leaving only fluctuations.[(5)]

It is possible that the decrease in level stems from hydrodynamic effects, decreasing with the downstream location as the turbulence eventually dies out. The difference in sound level between any two consecutive measurement planes in Figure 4.8 is approximately the same for all frequencies. Since dB is a logarithmic quantity, this indicates that the pressure fluctuations decrease by a factor rather than a constant; a decrease with any other appearance would affect the shape of the sound curves, changing it as the distance from the plate increases. This means that the decaying quantity has the same frequency spectrum as the sound generation mechanism. Consequently, if the decrease in sound level is due to turbulence, the turbulence must have the same frequency spectrum as the sound generation mechanism.

Another possible explanation is that the difference in level comes from some type of unphysical numerical efffect. To decrease the impact of such effects, the measurements should be taken as close to the plate as possible when the pressure has recovered. This is somewhat confirmed by Figure 4.8, where measurements close to the plate agree best with experiments. This study was limited by the fact that cross sections had to be created before the simulations. It is likely that the optimal cross section is located somewhere between the ones available.

A similar investigation as in Figure 4.8 was made for different upstream pressure measurement locations, however this showed that the upstream location does not

[(5)] For further details on how the sound was estimated, see Appendix D

significantly affect the sound estimate with respect to level or appearance. It can be concluded that the pressure drop begins after $x = -1D$, thus allowing for pressure estimation at any point further upstream.

4.5.1.1 Standard Deviation of Fluctuations

The sound level computed is connected to the amplitude of the pressure fluctuations, which can be quantified by means of the standard deviation σ. To further analyze the decrease in sound level the standard deviation for different cross sections is shown in Figure 4.9.

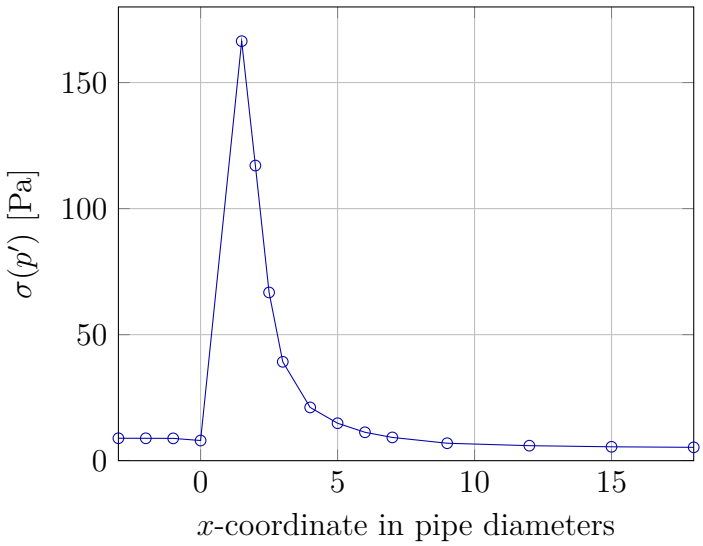

Figure 4.9: The standard deviation of the pressure fluctuation as a function of the measurement location, for the simulation of the stiff plate, with $M = 0.125$. The corresponding mean value can be seen in Figure 4.4a.

Upstream of the plate the standard deviation is approximately constant, $\sigma \approx 8$. Directly after the plate, the pressure fluctuation amplitude is drastically increased. However further downstream the fluctuation rapidly decreases, and the standard deviation reaches a new and lower constant level of $\sigma \approx 5$. The behaviour of the standard deviation resembles the behaviour of the pressure recovery, Figure 4.4: where the pressure drop is large, the standard deviation is also large, and vice versa. A difference is that the pressure drop has recovered at $x = 5D$ while the standard deviation stabilizes further downstream.

The standard deviation appears to be related to the difference in sound levels in Figure 4.8. Not only are they both decreasing downstream of the plate, the standard deviation also becomes constant around the location where the sound levels start to coincide. Above, it was mentioned that that this could be an effect of the outlet. The fact that the standard deviation approaches $\sigma = 5$ Pa somewhat contradicts this, since at the outlet the pressure is set to be constant and equal to zero, and hence the deviation must also be zero at the outlet.

4.5.2 Impact of Time Signal Length

The length of the time signal analyzed affects the results. In theory, the longer the time signal, the more accurate the estimate of the sound spectrum. It also means that longer time windows can be used, improving the frequency resolution.

To investigate how sensitive the spectrum is to the length of the time signal, computed spectra for three different signal lengths is presented in Figure 4.10.

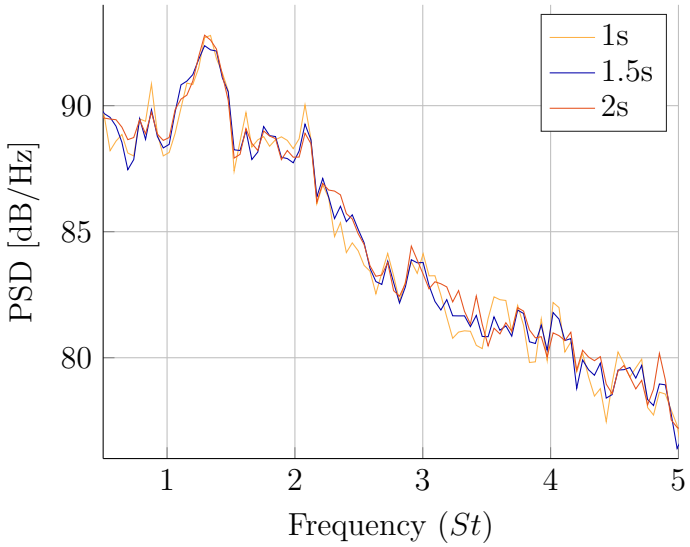

Figure 4.10: Investigation of the impact of signal length on the sound spectrum. The signals were taken from the simulation of the stiff plate at $M = 0.125$. The time in the legend is the total sample time used for analysis, and does not include the discarded first 0.5 s.

In general, the three spectra are quite similar both in terms of sound level and appearance. The shorter signal, with a length of 1 s, has larger variation. This is due to the low number of time sequences, n_d, available for computation of the autospectral density given that the sample length was kept constant at 2048 samples. If anything, using a longer signal will make the spectrum even smoother and no new peaks or dips in sound are thus to be expected for a longer time signal, as long as the frequency resolution is not changed. The 1.5 s signal lenght, which has been used for the majority of the analyses in the report, is therefore assumed long enough to aviod major errors.

4.5.3 Comparability to Experiments

The method used to estimate the sound spectrum in the experimental studies is not applicable to simulation counterparts. Hence, the sum of the upstream and downstream experimental sound measurements was chosen for comparison, as described in Section 2.4.5. In the previous numerical studies, however, there is no consensus regarding which experimental sound quantity to compare to. In Figure 4.11 the different experimentally measured sound estimates are compared to the simulated sound. Note that since the summation is done before the conversion to dB, the

difference between the compontents and their sum is fairly small. In this figure, the simulated sound and the sum of the experimental sound components are in good agreement.

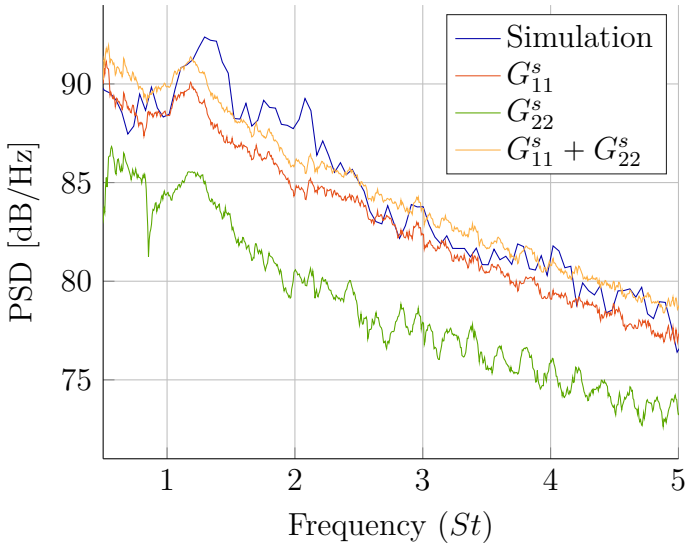

Figure 4.11: The experimentally measured upstream, downstream and total generated sound. Data from [3]. The sound estimate from the stiff plate simulation at $M = 0.125$ is included for comparison.

4.5.4 Scalability with Velocity

Experimental studies show that if the sound is scaled by u^4_{mean}, the sound curves for different mean velocities coincide [3]. To confirm the validity of this, a second velocity ($M = 0.188$) of the stiff plate case was simulated. Once again, the velocity choice is motivated by the existance of corresponding experimental data.

The increased velocity might change the pressure field in the duct, and hence the location of the cross section suitable for pressure measurements. However, studying the pressure recovery in the same way as in Section 4.3, it was concluded $x = 5D$ was a suitable choice also for this simulation. It can also be noted that although it recovered as rapidly, the pressure drop was increased for the higher velocity.

The resulting sound estimate is presented in Figure 4.12, toghether with equivalent results for the lower velocity of $M = 0.125$. The unscaled sound estimates are shown in Figure 4.12a, whereas Figure 4.12b presents the sound estimates scaled by the mean velocity to the power of four.

From Figure 4.12b, it can be concluded that the scaled sound curves coincide very well. Hence, it seems as if the simulated sound can also be scaled by u^4_{mean}. Remembering that dB is a logarithmic quantity makes the results even more remarkable. In the unscaled figure the higher velocity is also approximatly 6 dB louder, corresponding to a noise which is four times louder. After the scaling the difference is much smaller.

It is also interesting to note that, when plotting the frequency in terms of the Strouhal number, the trends of the sound curves coincide well. This would not have

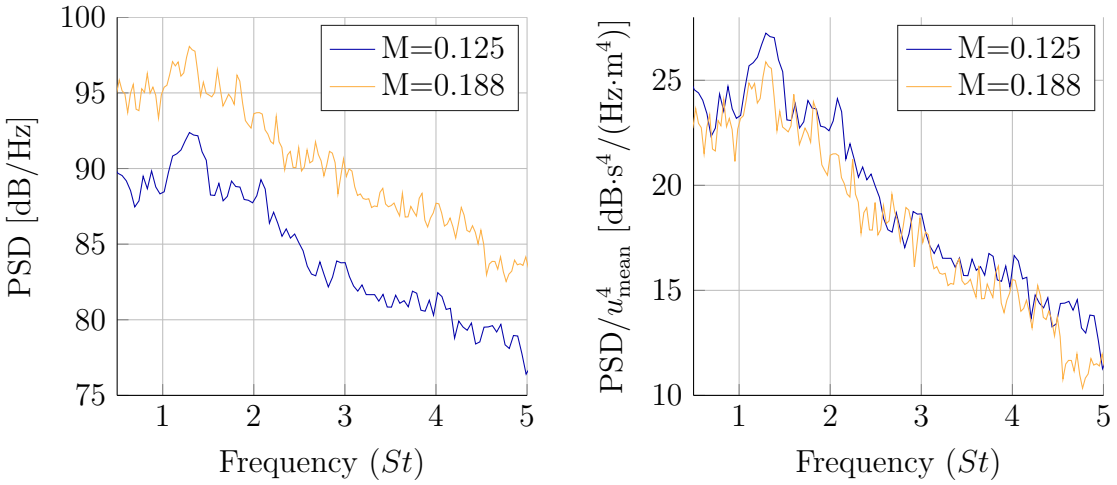

(a) PSD sound spectra for the stiff plate.

(b) PSD sound spectra for the stiff plate, scaled by u^4_{mean}.

Figure 4.12: Investigation of scalability of PSD sound estimate by mean velocity, for two velocities for the stiff plate case. The frequency resolution is 9.77 Hz in both cases.

been the case if the frequency had been expressed in Hertz, and indicates that a broadband noise peak at $St \approx 1.3$ is expected nonwithstanding of the mean flow velocity used.

4.6 Flow Physics

As a first step in the investigation of the flow, the Mach number is computed. In Section 3.2.2 the Mach number was computed as $M = 0.125$. However, this number is based on the mean velocity. To rule out compressibility effects, the Mach number based on the maximum velocity in the domain is needed. This is found in the narrow passage created by the plate and is approximately 94 m/s, which gives $M = 0.28$. Recalling that $M < 0.3$ is the recommended threshold, see Section 2.1, incompressibility is a valid approximation in the whole domain for the case with the low velocity.

For the case with the higher velocity, the mean Mach number is $M = 0.188$ but the maximum velocity is higher, $M \approx 0.41$. This exceeds the threshold of $M = 0.3$ for the incompressible flow assumption, meaning that results obtained from this simulation should be studied with some caution.

4.6.1 Velocity and Pressure Fields

In Figure 4.13, 2D contour plots of pressure and velocity in the symmetry plane of the stiff plate simulation with $M = 0.125$ are presented. The fields illustrate the chaotic behaviour of turbulence in the wake behind the plate quite well. Comparing the two subfigures, it is also clear that there is a large variation in the velocity and

pressure fields with time. In Figure 4.13a, a periodic creation of small low pressure areas after the plate can be noted, while in Figure 4.13b, there is a single large area of low pressure. The pressure is coupled to the velocity, meaning that also high velocity areas vary in size and distribution. However, even when investigating a large number of instantaneous velocity and pressure fields, recurring patterns that could be linked to the sound generation are not visible to the naked eye. Further analysis of possible noise generation mechanisms can be found in Section 4.6.2.

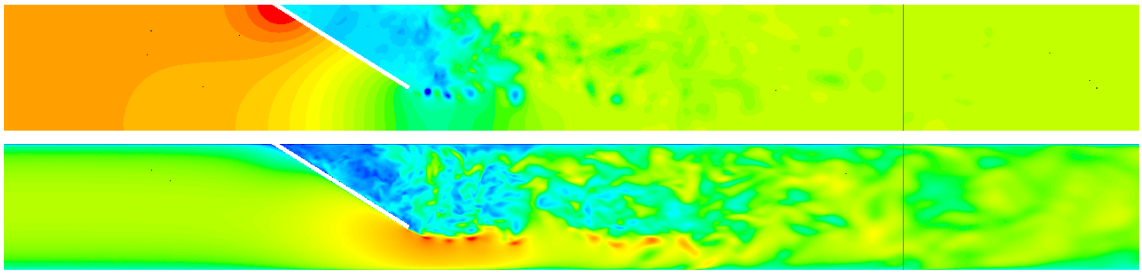

(a) Instantaneous pressure (top) and velocity (bottom) at $t = 1.9188$ s

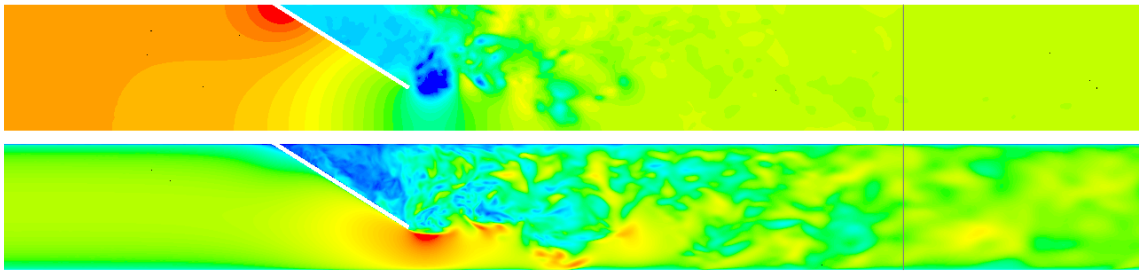

(b) Instantaneous pressure (top) and velocity (bottom) at $t = 1.9366$ s

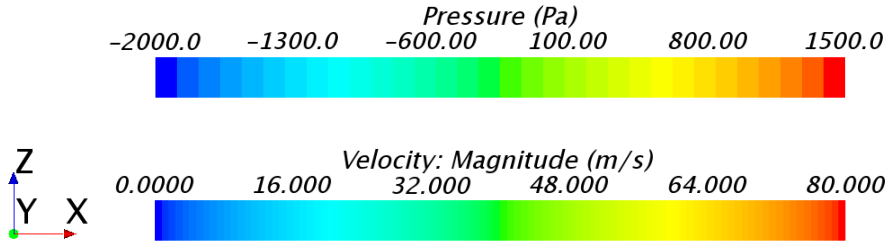

Figure 4.13: Pressure and velocity fields for the stiff plate at the symmetry plane of the domain ($y = 0$), for two different time steps. The mean Mach number is $M = 0.125$. Values above the maximum or below the minimum of the colour scale is shown as the maximum or minimum value respectively. Only a section ($x \approx -2D$ to $x \approx 7D$) of the domain is included. The gray vertical line marks $x = 5D$.

A closer look at the pressure contours reveals that the spatial variation in pressure downstream of $x = 5D$ is barely visible, especially in comparison with the variation before this coordinate. This indicates that $x = 5D$ is not too close to the plate and can be chosen as the downstream measurement location.

4.6.2 Sound Generation Mechanisms

It has been concluded that the plate contributes to the sound generation, see e.g. [1]. Since visual inspection does not reveal the mechanisms behind the sound generation, a more quantitative investigation of the pressure around the plate is made. The autospectral density is analyzed in some points just behind the plate edge, as described in Section 3.5.3. The autospectral densities for the points is presented in Figure 4.14. From the cross-spectral densities, the coherence and phase shift of the two signals (left and right point) of each pair are calculated, see Figure 4.15. For both figures, the x-axis has been limited to a range of Strouhal numbers where something of interest can be observed.

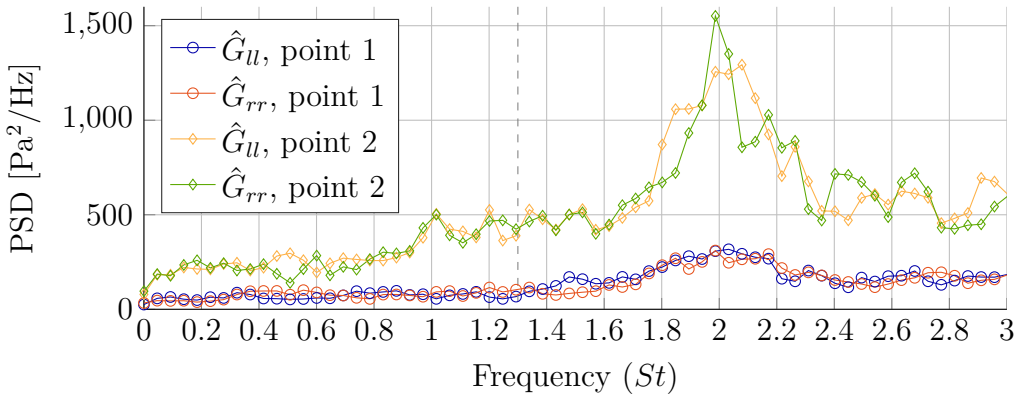

(a) Pressure fluctuation spectra from two pairs of measurement points placed close to the base of the plate. Their positions are visualized in Figure 3.9.

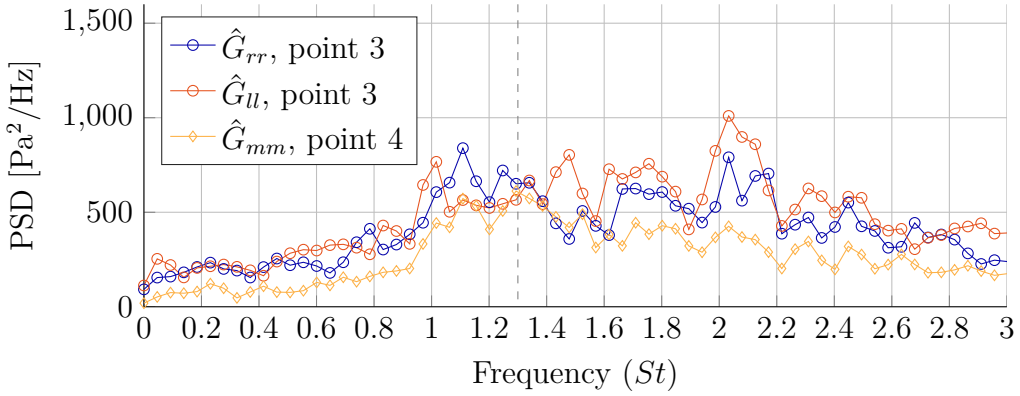

(b) Pressure fluctuation spectra for the last point pair and the single point at the tip of the plate.

Figure 4.14: Investigation of pressure fluctuations in points close to the stiff plate by autospectral density. Index m denotes middle, r right and l left. The dashed line marks the peak in the simulated sound estimate. Both plots have the same axes for easy comparison.

In Figure 4.14a a trend can be observed. Here, all autospectra have a peak at $St = 2$, indicating that this is a dominating frequency. The fact that the peak magnitude is lower in point pair 1 is probably due to wall effects. Studying corresponding

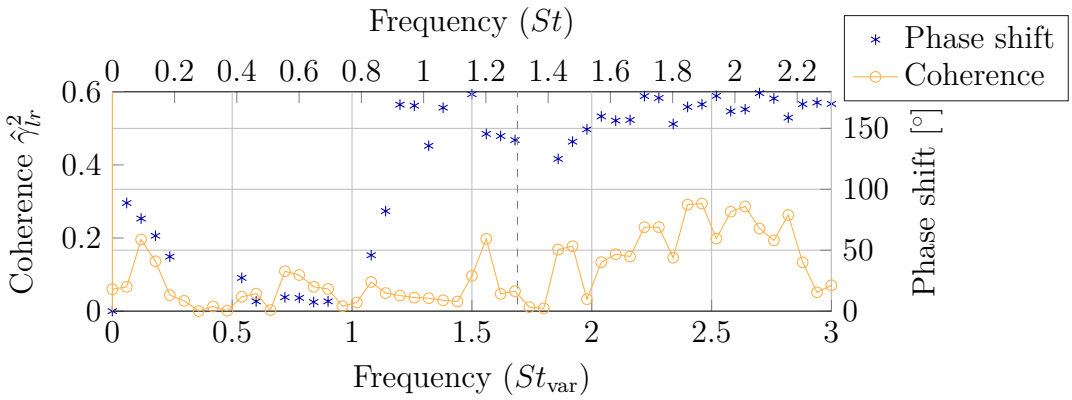

(a) Point pair 1, defined as 1 in Figure 3.9.

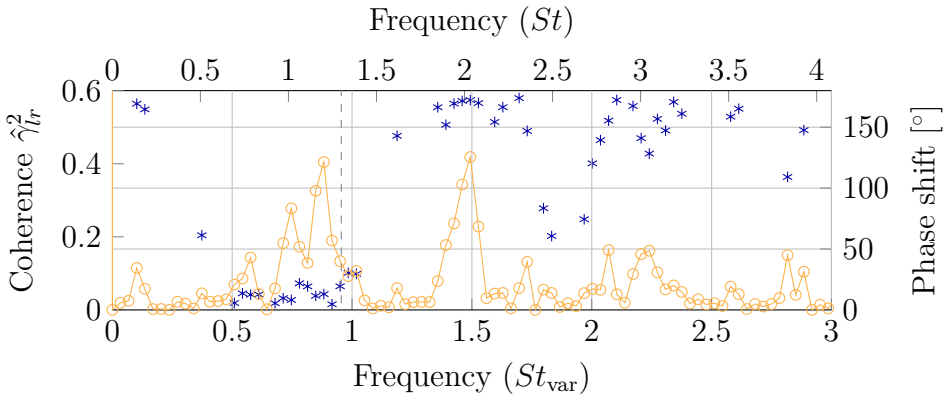

(b) Point pair 2.

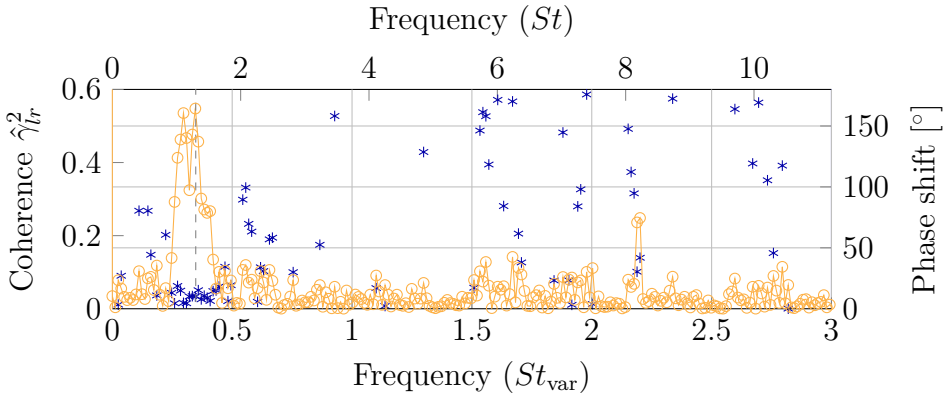

(c) Point pair 3.

Figure 4.15: Investigation of pressure fluctuations in points close to the stiff plate, in terms of coherence and phase shift. Indices r and l denote right and left respectively. For the phase shift the absolute value is used, and values corresponding to very low coherence have been removed. The top x-axis shows St based on $\ell = 0.032$ m and $u = u_{\text{mean}}$ as in previous figures, while the bottom x-axis shows a Strouhal number St_{var} that is dependent on plate width and local velocity, see Table 3.2. The dashed line marks the peak in the simulation sound estimate. The legend is common for all subplots.

coherence and phase shift, Figure 4.15a and 4.15b, it can be noted that there is a phase shift of about 180° at this frequency for both point pairs.

Studying the phase shift in Figures 4.15a and 4.15b, common behaviours can be found when scaling with the alternative Strouhal number. For $0.5 < St_{\text{var}} < 1$ the phase shift is 0°, meaning that the pressure fluctuations are in phase. Above this the phase shift is instead 180° indicating that the pressure fluctuations are now in antiphase. In the last coherence plot, Figure 4.15c, this trend is not seen. However, it should be noted that the coherence is relatively low in all figures.

Moving on to Figure 4.14b, and point pair 3, the peak around $St = 2$ has become considerably lower, such that this is no longer a clearly dominating frequency. Instead, a broadband spectrum between the Strouhal numbers 1 and 2.2 has emerged. Comparing with the coherence in Figure 4.15c it is obvious that a new peak, with a stronger coherence has emerged at $St \approx 1.2$. This peak was present already in Figure 4.15b, and it is in phase. Another interesting observation in Figure 4.15c is that the phase shift for $St = 2$ has changed, and is now approximately 90° instead of 180°, although the coherence is fairly low.

The furthest downstream monitor location has only a single point, since the pairs of points meet there. Having only one point, it is not possible to calculate the cross-correlation or coherence, but the autospectral density shows that the broadband spectrum is still present, see Figure 4.14b. Its highest peak is centered around $St \approx 1.3$, which is the same frequency as the peak in the estimated sound spectra for the stiff plate, see Figure 4.6a.

The periodicity and the antiphase behaviour shown in Figure 4.14a is probably the effect of a von Kármán vortex street. It is characterized by periodic shedding, where vortices are alternately created at the opposite edges of the body. When the plate width decreases, towards the tip, the horizontal distance between the points in a pair also decreases. It is possible that this decrease in distance is causing the decrease in phase shift. Instead the dominating sound frequency emerges behind the plate tip. This could indicate that this is where the peak in the sound spectrum arises.

A similar investigation was made for the flexible plate. It showed no major differences compared to the stiff plate case. However, as seen in Figure 4.16, the autocorrelation of the point near the middle of the plate shows that the noise content at the peak at $St \approx 2$ is slightly reduced when a flexible plate is introduced. The peak also has a more broadband character.

4.7 Fluid Mesh Strategy and Dependency

For the geometry at hand it was unexpectedly difficult to create a high quality mesh. The tip and the back of the plate near the wall are areas in which the normal automated mesh tools perform poorly unless a number of additional settings are made.

The plate tip is a very important region; the velocity is high and it is presumably important for sound generation. The difficulty in creating a well performing mesh stems from the sharp corner at the plate tip causing problems in the prism cell generation. As mentioned in Section 3.2.1, it was found that the Advancing Layer

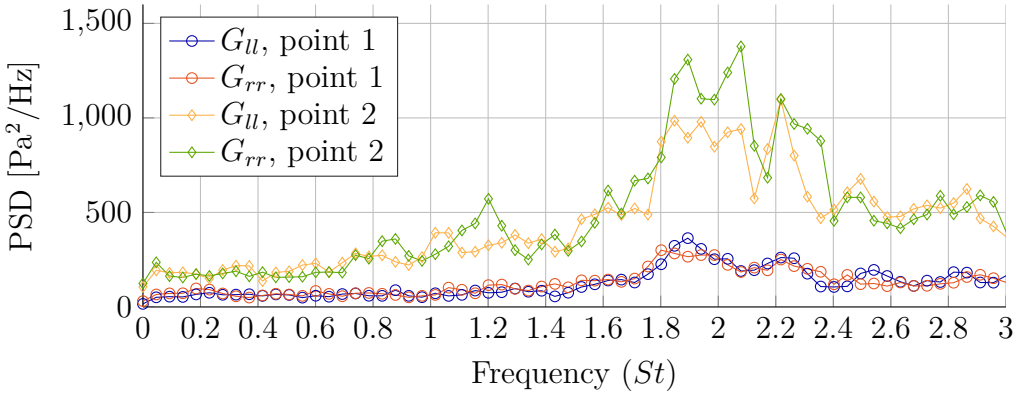

Figure 4.16: Pressure fluctuation spectra for the flexible plate case, from two pairs of measurement points placed at the base of the plate. The position of the pairs is visualized in Figure 3.9.

Mesher created fewer skew or disproportionally large cells than the more commonly used Prism Layer Mesher, and therefore it was used.

In the other problematic area, at the plate back just where the plate meets the wall, prism cells with large skewness or poor aspect ratio tend to form. From a numerical perspective, it is problematic if the combined center of mass of two adjacent cells is not located within the cells in question. This problem was indeed present here, and might have been the cause of divergence problems experienced. Using the Advancing Layer Mesher the only way found to remedy the cell quality problems was to drastically lower the cell size in the region. Since the flow has a very low velocity here, and therefore probably does not contribute much to the general flow, the refinement was kept at a level as moderate as possible[(6)].

An alternative solution to both mesh problems mentioned could be to round off complicated sharp edges. This was considered, but the technique has a number of drawbacks. First, a change in the geometry would constitute a source of error when comparing to results from the experimental study. Secondly, it would complicate the setup of the flexible plate case, since the plate and fluid surfaces at interfaces would not have a 100% match.

Initially, two meshes of different cell count were created, to investigate the independence of the solution with respect to the mesh. Unfortunately, the less fine mesh resulted in divergence, probably due to numerical effects. Thus only the finest mesh was used for simulations. This mesh, as mentioned in Section 3.2.1, contained almost 10^7 cells and the simulations were carried out using a cluster with 120 CPUs. With a recommendation of 10^5 cells per CPU, there was thus quite limited room for further refinements without drastically increasing the required simulation time [11].

4.8 Star CCM+ Fluid-Structure Interaction

Given the difference in sound generation of the FSI simulation and the experimental results, see Section 4.5, some aspects of the solver were studied further.

[(6)] For a visual representation, see Figure A.2

In the plate mesh independency study, described in Section 3.3.1, all meshes gave a deflection of almost 2.4 mm. The conformity in deflection indicated that the plate mesh used was fine enough. Since the modal analysis performed (see Section 4.1) confirmed that the material properties of the solid were reasonable, it seems that the model of the plate should not be the reason for the unexpected results.

Even if the plate model is assumed to be accurate, there are still doubts regarding the correctness of the plate displacement, which as discussed in Section 4.3.1 appears to be at a bare minimum compared to the value estimated from [2]. The problems might be caused by an inaccurate load from the surrounding flow. Thus, a study on how the fluid mesh refinement affected the displacement was performed. In the study the fine fluid mesh used for simulation was compared to a much coarser test grid, with a base size of around 0.0018 m around the plate[7]. Once again, a static FSI simulation was performed, and no difference in plate deflection was found.

However, the cell size is not the only important parameter in creating an adequate mesh. It is also important that the cells have a reasonable aspect ratio, that the difference in volume between adjacent cells is acceptable etc. The mesh must remain high quality also when it is recomputed due to the plate motion. In Star CCM+, it is possible to always recompute the mesh starting from its original state instead of from the previous mesh, an option called Morph from Zero. The effect of this option was evaluated by comparing two transient simulations on a coarse test mesh. The simulations were identical except for the activation of Morph from Zero, see Figure 4.17. The option proved to have a clear impact on the plate vibration. At first, the difference is small but as the solver advances, the solutions differ more and more. Since the difference is non-negligible and Morph from Zero is recommended for periodic motions [11], and thus in our case presumably more exact, it was used in the simulation from which the flexible plate results are extracted. It can also be noted that the option had negligible impact on the computational time for the test case.

Another option in the FSI solver is to make the problem strongly or weakly coupled, see Section 2.3. A weakly coupled approach was chosen, since this should in theory be sufficient and reduce the computational time. For verification, an investigation similar to the one on Morph from Zero was performed. The result showed that there was no significant difference in plate tip displacement depending on whether a strong or a loose coupling was chosen, but that the weakly coupled case required less simulation time.

Even after investigation of the above settings, the results indicate that the plate does not deflect as much as expected. One possible explanation is that the plate model is too stiff, which can occur if the solid mesh quality is low. However, as mentioned in Section 4.1, a too stiff plate model would also affect the modes, which were confirmed to be accurate. Additionally, the mesh independency study suggested that the plate mesh used was fine enough. Another explanation could be that the the flow is incorrectly predicted, which would in turn affect the plate, but no indications of this were found. Finally, the explanation to the underpredicted deflection might be a problem in the FSI solver, possibly with the transfer of forces at the interfaces.

All in all, though the plate displacement is smaller than desired, the FSI has

[7] The fine mesh used has a Base size of 0.001 around the plate

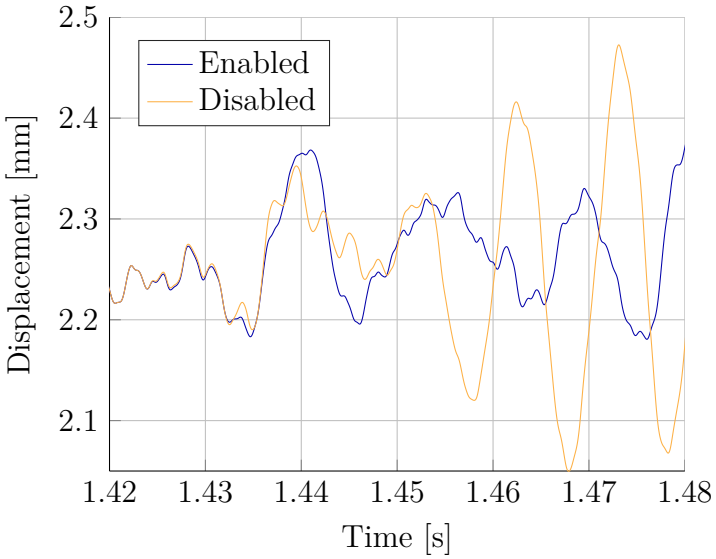

Figure 4.17: Effect of Morph from Zero on tip displacement. The two cases were started from an identical FSI simulation on a coarse test mesh. The option Morph from Zero was enabled in one of the cases around $t = 1.425$ s.

predicted the plate motion accuratley. Fundamental frequencies, which are probably more important for the problem at hand, were captured and agreed with the available reference values.

4.9 Validity of the Dipole Sound Approximation

Assuming that the Star CCM+ FSI solver accurately captures the physics of the flexible plate problem, the discrepancy in estimated sound between simulations and experiments must be caused by some other factor. Although the dipole sound approximation (Equation 2.18) seems to be valid in the stiff plate case, it is not sure that it is applicable to the flexible plate case. It might be necessary to use the regular, unsimplified, version of Curle's equation or another method to capture the sound reduction.

The dipole approximation used is a greatly simplified method for sound estimation. The fact that this crude estimation cannot capture all sound generation mechanisms does not seem improbable. Apparently, a mechanism which is not present in the stiff plate case causes a reduction in sound for the flexible plate case. By analyzing the approximation with respect to uncapturable mechanisms some understanding of the sound reduction can still be obtained.

The results indicate that the sound source term which can be captured by the dipole approximation, is uncoupled to the plate movement. Hence the plate movement can be introduced without affecting the sound estimation. If anything it seems like the flexible plate has a sound increase effect at the expected sound reduction frequency.

5
Conclusion

Using Star CCM+ and applying the dipole sound approximation, it is possible to accurately predict the sound generated by a stiff vortex mixer plate. However, it was found that it is essential to measure pressure fluctuations with great attention, since the results are heavily dependent on measurement location. It is also possible to accurately predict the velocity profiles in the duct. Indications of the dominating sound frequency being generated near the plate tip were found.

Furthermore, the Star CCM+ Fluid-Structure Interaction solver performs well when it comes to solving the flow induced vibration of the plate, but slightly underpredicts the defelction. For the flexible plate, the estimated sound does not include trends expected from the experimental results, which might be due to the application of the dipole sound approximation. It was also found that when scaled with velocity the PSD sound estimates, as a function of the Strouhal number, coincides for simulations with different mean velocity.

5.1 Future Work

Given the doubts regarding the use of the dipole sound approximation in the flexible plate case, a first step might be to run an additional FSI simulation, and use for example the original Curle's analogy to estimate sound to see if the sound reduction can be captured. Another valuable supplement to the present work would be the performance of a fluid mesh independency study. It could also be interesting to test different turbulence models and see if the wall treatment can be improved.

Bibliography

[1] A. Holmberg. "An aero-acoustic study of an in-duct flexible plate". Stockholm: Kungliga Tekniska högskolan, 2008.

[2] M. Karlsson, A. Holmberg, M. Åbom, B. Fallenius, and J. Fransson. "Experimental determination of the aero-acoustic properties of an in-duct flexible plate". *14th AIAA/CEAS Aeroacoustics Conference (29th AIAA Aeroacoustics Conference)* (2008).

[3] A. Nöjd. Internal communication. 2016.

[4] J. Jansson, A. Holmberg, R. Vilela de Abreu, C. Degirmenci, J. Hoffman, M. Karlsson, and M. Åbom. "Adaptive stabilized finite element framework for simulation of vocal fold turbulent fluid-structure interaction". *Proceedings of Meetings on Acoustics, 035041 (2013)* 19 (2013). Ed. by Acoustical Science of America.

[5] R. Vilela de Abreu, J. Hoffman, and J. Jansson. "Towards the Development of Adaptive Finite Element Methods for Internal Flow Aeroacoustics". *19th AIAA/CEAS Aeroacoustics Conference* (2013).

[6] F. M. White. *Fluid mechanics*. 7th ed. in SI units. Singapore: McGraw-Hill, 2011.

[7] P. Sagaut, S. Deck, and M. Terracol. *Multiscale and multiresolution approaches in turbulence: LES, DES and hybrid RANS/LES methods : applications and guidelines*. 2nd ed. London: Imperial College Press, 2013.

[8] H. K. Versteeg and W. Malalasekera. *An introduction to computational fluid dynamics: the finite volume method*. 2nd ed. Harlow: Pearson Prentice Hall, 2007.

[9] A. Dewan. *Tackling turbulent flows in engineering*. 1st ed. Berlin: Springer, 2011.

[10] G. Iaccarino, A. Ooi, P. A. Durbin, and M. Behnia. "Reynolds averaged simulation of unsteady separated flow". *International Journal of Heat and Fluid Flow* 24.2 (2003), pp. 147–156.

[11] Star CCM+ *User Guide*. CD-adapco. 2016.

[12] H. Lundh. *Grundläggande hållfasthetslära*. 3rd revised ed. Stockholm: Institutionen för hållfasthetslära, Kungliga Tekniska högskolan, 2000.

[13] L. P. Lebedev, M. J. Cloud, and V. A. Eremeyev. *Tensor analysis with applications in mechanics*. New Jersey: World Scientific, 2010.

[14] N. Ottosen and H. Peterson. *Introduction to the Finite Element Method*. New York: Pearson Prentice Hall, 1992.

[15] J. He and Z.-F. Fu. *Modal analysis*. New ed. Oxford: Butterworth-Heinemann, 2001.

[16] Y. Bazilevs, K. Takizawa, and T. E. Tezduyar. *Computational fluid-structure interaction: methods and applications*. Hoboken, N.J: Wiley, 2013.

[17] M. Möser. *Engineering acoustics: an introduction to noise control*. 2nd ed. Berlin: Springer, 2009.

[18] M. Åbom. *An Introduction to Flow Acoustics*. 4th ed. Stockholm: Kungliga Tekniska högskolan, 2006. URL: `https://www.dropbox.com/s/e2tyf94i4rymvru/SD2155%20FlowAc.pdf?dl=0`.

[19] G. B. Folland. *Fourier analysis and its applications*. 4th ed. Providence, R.I: American Mathematical Society, 2009.

[20] J. S. Bendat and A. G. Piersol. *Engineering applications of correlation and spectral analysis*. 2nd ed. New York: Wiley, 1993.

[21] P. Welch. "The use of fast Fourier transform for the estimation of power spectra: A method based on time averaging over short, modified periodograms". *IEEE Transactions on Audio and Electroacoustics* 15.2 (1967), pp. 70–73.

[22] M. H. Trauth, R. Gebbers, and N. Marwan. *MATLAB recipes for earth sciences*. 2nd ed. Berlin: Springer, 2007.

Appendix

A Mesh Details

All settings made in STAR CCM+ to generate the meshes used in the thesis, and some additional graphics, are presented below.

Table A.1: All customized settings done to accomplish the mesh in the fluid domain. For definition of plate surfaces see Figure 3.3.

Parameter	**Settings**
Meshers	Surface Remesher Polyhedral Mesher Advancing Layer Mesher
Default controls	Base size: 0.002 m Surface Growth Rate: 1.2 Number of Prism Layers: 14 Prism Layer Total Thickness: 100% of base size Prism Layer Stretching: 1.4 Mesh Density Growth Factor: 0.5
Volume control, refinement cylinder	Surface Remesher: Enabled Customize Polyhedral Mesher: Enabled ↳ Custom size: 50% of base size
Volume control, cylinder with increased mesh size	Surface Remesher: Enabled Customize Polyhedral Mesher: Enabled ↳ Custom size: 120% of base size
Surface control, plate front	Surface Remesher: Enabled Target Surface Size: 25% of base size Number of Prism Layers: 13 Prism Layer Total Thickness: 50% of base size
Surface control, plate back	Surface Remesher: Enabled Target Surface Size: 25% of base size Number of Prism Layers: 11 Prism Layer Total Thickness: 50% of base size
Surface control, plate edges	Surface Remesher: Enabled Target Surface Size: 25% of base size Number of Prism Layers: 11 Prism Layer Total Thickness: 50% of base size

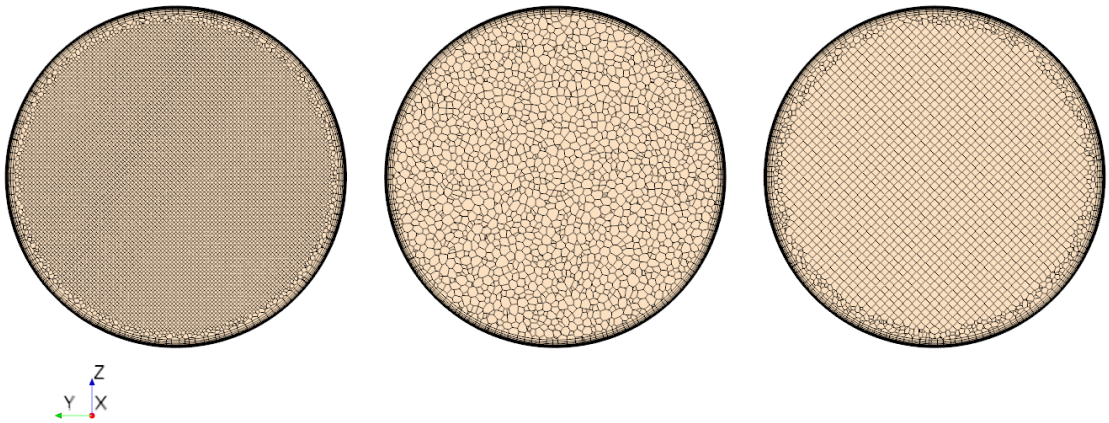

Figure A.1: Fluid mesh in three cross sections, to the left the fine mesh of the area near the plate, in the middle the mesh used in the majority of the domain and to the right the coarse mesh close to the outlet.

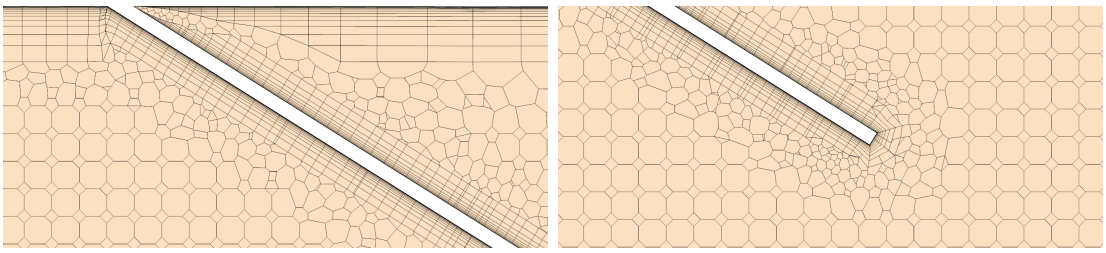

Figure A.2: Zoom in of the mesh around the problematic areas for the flexible (0.5 mm) plate: the intersection of the plate and the pipe where some poor quality cells were located (left) and the region around the plate tip (right). The mesh is oriented as in Figure 3.4. The same scale is applied to both subfigures.

Table A.2: All customized settings for creation of mesh in the solid domain.

Parameter	**Settings**
Meshers	Surface Remesher Tetrahedral Mesher Thin Mesher
Default controls	Base size: 0.01 m Number of Thin Layers: 2

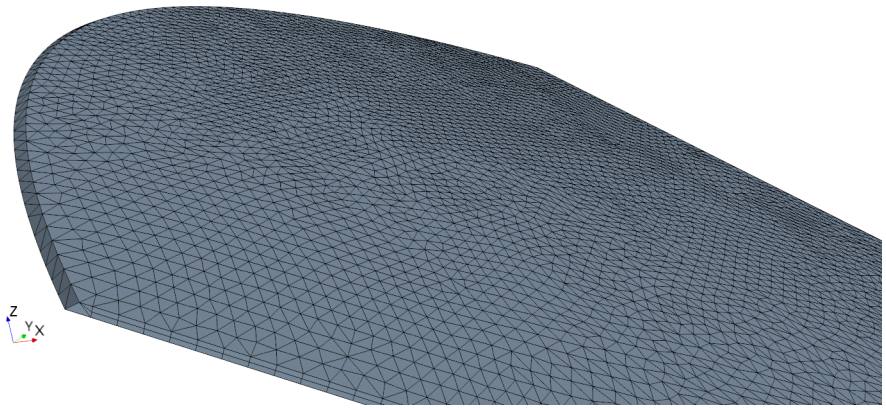

Figure A.3: The solid mesh seen from the top corner of the plate.

B Detailed Simulation Setup Parameters

The following settings were made for the different simulations in Star CCM+. The *physics model* governs certain properties of and methods used on a continuum, while details regarding how the discretized equations are solved are set under *solvers*. Where no value or setting is specified, the default was used.

B.1 Physics models

Table B.1: Steady simulation model (RANS) used to obtain initial conditions for transient simulation.

Model	**Settings**
Three Dimensional	
Steady	
Gas	Air
Segregated Flow	
Gradients	
Constant Density	
Turbulent	
Reynolds-Averaged Navier Stokes	
K-Epsilon Turbulence	
Realizable K-Epsilon Two-Layer	
Exact Wall Distance	
Two Layer All y+ Wall Treatment	
Cell Quality Remediation	

Table B.2: Transient simulation physics model: Detached Eddy Simulation.

Model	**Settings**
Three Dimensional	
Implicit Unsteady	
Gas	Air
Segregated flow	Convection scheme: Hybrid MUSCL 3rd order/CD Secondary gradients: Enabled
Gradients	Limiter method: Use TVB Gradient Limiting Acceptable field variation: 0.15
Constant Density	
Turbulent	
Detached Eddy Simulation	
Spalart-Allmaras Detached Eddy	
Exact Wall Distance	
All y+ Wall Treatment	
Cell Quality Remediation	

Table B.3: Physics model settings for static solid simulations.

Model	**Settings**
Three Dimensional	
Solid	Carbon Steel, UNSG101000
Solid Stress	
Linear Isotropic Elastic	
Steady	
Fluid Structure Coupling	

Table B.4: Physics model settings for transient solid simulations. *Used for FSI simulations only, i.e. not in the modal analysis.

Model	**Settings**
Three Dimensional	
Solid	Carbon Steel, UNSG101000
Solid Stress	
Linear Isotropic Elastic	
Implicit Unsteady	
Fluid Structure Coupling*	

B.2 Solvers

Table B.5: Solver settings for the transient stiff plate problem.

Solver	**Settings**
Implicit Unsteady	Time-Step: $5 \cdot 10^{-5}$ Temporal Discretization: 2nd-order
Segregated Flow	
Velocity	Under-Relaxation Factor: 0.7
Pressure	Under-Relaxation Factor: 0.7 AMG Linear Solver, Max Cycles: 50 AMG Linear Solver, Cycle Type: F-cycle

Table B.6: Solver settings for the transient FSI problem.

Solver	**Settings**
Implicit Unsteady	Time-Step: $5 \cdot 10^{-5}$ Temporal Discretization: 2nd-order
Fluid Structure Interaction	Method: Two-Way FSI Displacement Convergence Tolerance: 1
Mesh Morpher	Morph From Zero: Enabled
Segregated Flow	
Velocity	Under-Relaxation Factor: 0.7
Pressure	Under-Relaxation Factor: 0.8 AMG Linear Solver, Max Cycles: 50

C Drag Coefficient Calculations

C.1 Experimental Drag Coefficients

The drag coefficient values from the two experimental studies [1, 2], although beyond reasonable doubt computed from the same pressure drop values, differ by a factor of 0.8. In addition to this, possible errors were detected in the computations in [1]. After concluding that the scaling in [2] most probably did not compensate for this, a decision was made to recompute the drag coefficients using the pressure drop measurements, see Table C.1. The drag coefficients from the simulations were then compared to the recomputed drag coefficients instead of the ones given in the mentioned sources.

Table C.1: Experimental measurements of pressure loss in an empty plastic pipe over a length $\Delta L = 3.081$ m. Values from [1].

Centerline velocity [m/s]	Pressure loss [Pa]
29.0	210
34.7	290
58.0	770
68.0	1060
84.5	1600
102.0	2320

Using the pressure loss measurements for the empty plastic pipe and assuming that the loss is caused by friction, the friction factor can be computed according to

$$c_f = \frac{\Delta p D}{2\rho u^2 \Delta L} \tag{C.1}$$

where the velocity used is the mean velocity, in this case given by the centerline velocity times a scaling constant of 0.82, and $D = 0.09$ m is the diameter of the duct. In this case the density $\rho = 1.2$ kg/m^3 [1]. The equation gives different friction factor values for the different velocity measurements. Evaluating all velocities, the mean friction factor is $c_f = 4.21 \cdot 10^{-3}$. Solving Equation C.1 for Δp for the mean velocity of interest, the pressure loss due to friction is found. Subtracting this from the total pressure loss, the decrease in pressure due to the plate is obtained. The results for the cases of interest are collected in Table C.2.

C.2 Projected Area

A correctly calculated projected area A_{proj} is key to obtain a comparable drag coefficient. A_{proj} can be seen as the sum of a triangular surface and a circle segment. Using the measurements from Figure C.1, the area of the triangular part is $1.52 \cdot 10^{-3}$ m^2. The circle segment area is computed from

$$A_{\text{circSeg}} = \frac{r^2}{2}(\alpha - \sin\alpha) \tag{C.2}$$

Table C.2: The pressure losses obtained for the cases where simulation data to compare with exist. Δp_{total} is the pressure loss measured. $\Delta p_{\text{friction}}$ refers to the pressure loss due to wall friction for the specific velocity, calculated via c_f. Finally for Δp_{plate} the pressure loss wall friction has been subtracted from the total pressure loss.

Plate thickness [mm]	Centerline velocity [m/s]	Mean velocity [m/s]	Δp_{total} [Pa]	$\Delta p_{\text{friction}}$ [Pa]	Δp_{plate} [Pa]
3	51.9	42.56	1250	626.60	623.40
0.5	52	42.64	1170	620.71	549.29

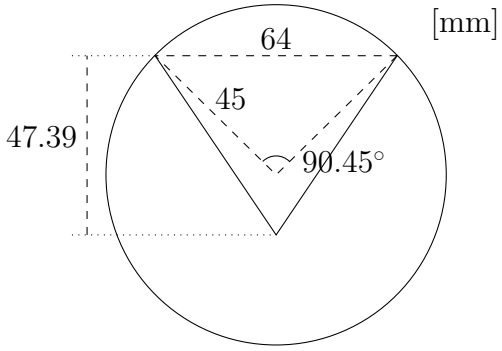

Figure C.1: The plate as it appears when projected in the streamwise direction. The dashed lines mark reference lengths used to compute the area. The height of 47.39 mm was computed using the dimensions and the angle of the plate, see Figure 3.2.

where α is the midpoint angle (see Figure C.1) expressed in radians. The area of the circle segment becomes $5.89 \cdot 10^{-4}$ m^2. This gives a total projected area $A_{\text{proj}} = 2.1 \cdot 10^{-3}$ m^2. The projected area of the duct is $A_{\text{duct}} = 6.36 \cdot 10^{-3}$ m^2.

D Matlab Code for Sound Estimation

```
clc, clear all, close all

% --- Change these variables if needed ---
pressFile = 'fileName.csv'; % Pressure, averaged over pipe cross sec

startpoint = 10000; % Omit first 0.5 sec
uMean = 42.5; % Based on known mass flow rate, for u_centerline = 50m/s
charLength = 0.032; % Characteristic length [m], for St calc.
NFFTfactor = 2; % Affects frequency resolution + number of windows

% Constants
p0 = 2e-5; % [Pa], reference pressure for dB

% --- Use the above to estimate sound generation ---
pressureData = csvread(pressFile,1,0); % Read physical time,
    % average surface pressures upstream and downstream of plate

timeVec = pressureData(startpoint:end,1);
xmin2 = pressureData(startpoint:end,3);
x5D = pressureData(startpoint:end,10);

pDown = x5D; % Downstream pressure
pUp = xmin2; % Upstream pressure
pressFluct = pUp-pDown;

dt = mean(diff(timeVec)); % Find time step
Fs = 1/dt; % Sampling frequency

NFFT = 1024*NFFTfactor; % Window length
df = 1/NFFT/dt; % Resulting frequency resolution
numWindows = floor(2*(length(timeVec)/NFFT)-1); % Approx

window = hanning(NFFT);
pressFluct = pressFluct-mean(pressFluct);
    % Center fluctuations around 0
[Pxx,f] = pwelch(pressFluct,window,NFFT/2,NFFT,Fs);
    % Computes autospectral density function via Welch method

st = 2*pi*f*charLength/uMean;
lp = 10*log10(Pxx/p0^2);
lpscaled = 10*log10(Pxx/p0^2/uMean^4);
```